UNIVERSIDADE D
COIMBRA

António Francisco de André Girão Neto Parra

Drug encapsulation in extracellular vesicles for Age-related Macular Degeneration treatment

Dissertation presented to the University of Coimbra as a requirement for the degree of MSc in Biomedical Engineering and performed under the supervision of Doctor Rosa Cristina Simões Fernandes, Auxiliary Investigator at the Faculty of Medicine of the University of Coimbra, and Doctor António Francisco Rosa Gomes Ambrósio, Coordinator Investigator at the Faculty of Medicine of the University of Coimbra

October, 2021

UNIVERSIDADE D
COIMBRA

António Francisco de André Girão Neto Parra

DRUG ENCAPSULATION IN EXTRACELLULAR VESICLES FOR AGE-RELATED MACULAR DEGENERATION TREATMENT

Dissertation presented to the University of Coimbra as a requirement for the degree of MSc in Biomedical Engineering and performed under the supervision of Doctor Rosa Cristina Simões Fernandes, Auxiliary Investigator at the Faculty of Medicine of the University of Coimbra, and Doctor António Francisco Rosa Gomes Ambrósio, Coordinator Investigator at the Faculty of Medicine of the University of Coimbra

October, 2021

Support

This work was carried out at the Coimbra Institute for Clinical and Biomedical Research (iCBR), Faculty of Medicine, University of Coimbra, Portugal, in collaboration with the Centro de Química Estrutural (CQE), Chemical Engineering Department, Instituto Superior Técnico, University of Lisbon, Portugal.

The work was supported by the Foundation for Science and Technology (FCT), through the Strategic Project UIDB/04539/2020 and UIDP/04539/2020, and by Centro 2020 Portugal Regional Operational Programme (CENTRO-01-0145-FEDER-000008; Brain Health 2020).

Agradecimentos

Bem, que ano! Sem dúvida, o mais desafiante da minha vida. Foi um percurso de enorme aprendizagem, a todos os níveis, e não se concretizaria sem a ajuda dos meus colegas, família e amigos. Por isso mesmo, reservo este pedaço da minha tese para os que me ajudaram a chegar ao momento em que vos escrevo.

Em primeiro lugar, gostaria de agradecer aos meus colegas do iCBR, um excelente grupo de seres humanos, que se pautam pela educação, pela entreajuda e por uma enorme curiosidade científica. Gostaria de destacar o papel fundamental da Dra. Rosa Fernandes, a minha orientadora e a mentora deste projeto. Não só o idealizou, como foi incansável em ajudar-me no seu desenvolvimento e na escrita desta mesma tese. Palavras não chegam para lhe agradecer devidamente. Ao Dr. Francisco Ambrósio, o coorientador deste trabalho, gostaria de agradecer o contributo que deu em cada reunião, encontro fortuito, …, essenciais para o desenvolvimento e conclusão deste projeto. Ao Dr. João Tomé, que nunca cheguei a ter o prazer de conhecer em pessoa, mas que também me ajudou bastante na compreensão do fármaco usado neste trabalho, desenvolvido pela sua equipa. À Beatriz Martins, uma colega que me ensinou imenso, a nível profissional e pessoal, e que sempre foi proativa e disponível para me ajudar neste projeto. À Joana Martins, com quem trabalhei para estabelecer o modelo animal, gostaria de dizer que foi uma colega de excelência com quem partilhei preciosos momentos de amizade que levo comigo para a vida. Gostaria ainda de sublinhar os contributos da Andreia Melo, da Maria Pires e da Sandra Beirão, mulheres fantásticas com quem tive o prazer de trabalhar em proximidade no último ano.

Quanto à família e amigos, deixo-vos uma nota breve, porque vocês sabem quem são e o quanto gosto de cada um. À minha mãe, pai, irmãos e namorada, um agradecimento muito especial, por todo o vosso apoio e paciência, fundamentais para a conquista desta etapa da minha vida. Aos amigos, por caminharem a meu lado, certificando-se constantemente que me mantenho no caminho certo. A minha motivação para realizar este trabalho não foi somente egoísta, porque tenho a felicidade de vos ter na minha vida e todo o prazer em deixar-vos orgulhosos de mim.

Table of Contents

Abbreviations xi
Abstract xiii
Resumo xv
Chapter I: Introduction 1
1.1 The Human Eye 3
1.1.1 Anterior Segment 3
1.1.2 Posterior Segment 4
1.1.2.1 Retina 5
1.2 Age-Related Macular Degeneration (AMD) 7
1.2.1 Pathology 7
1.2.2 Prevalence and Risk Factors 9
1.2.3 Galectins in Wet AMD 9
1.2.4 Current Therapies 10
1.2.4.1 Early and Intermediate AMD 10
1.2.4.2 Dry AMD 11
1.2.4.3 Wet AMD 11
1.3 Photodynamic Therapy (PDT) 12
1.3.1 Principle of PDT and its Applications 12
1.3.1.1 Type I Photochemical Reaction 13
1.3.1.2 Type II Photochemical Reaction 13
1.3.2 Photosensitizers (PS) 14
1.4 Drug Encapsulation in Extracellular Vesicles 15
1.4.1 Extracellular Vesicles (EVs) 15
1.4.2 Drug Loading Methods 15
1.4.3 Applications 17
1.5 Animal Model for CNV Induction 17
1.6 Objectives 18
Chapter II: Materials and Methods 21
2.1. Preparation of $ZnTPPF_{16}(SGal)_4$ 23
2.2 Visible Characterization of $ZnTPPF_{16}(SGal)_4$ 23
2.3 Photostability Assay 23
2.4 Isolation of Exosomes from Porcine Eyecups 23
2.5 $ZnTPPF_{16}(SGal)_4$ Loading into Exosomes 24
2.6 Protein Quantification 24
2.7 Nanoparticle Tracking Analysis (NTA) 25

2.8 Transmission Electron Microscopy (TEM) 25
2.9 Cell Culture and Maintenance 25
2.10 Incubation of ARPE-19 Cells with $ZnTPPF_{16}(SGal)_4$ and Exosomal $ZnTPPF_{16}(SGal)_4$ 26
2.11 Determination of Intracellular Concentration of $ZnTPPF_{16}(SGal)_4$ 26
2.12 Photodynamic Assays 26
2.13 ARPE-19 Cell Viability Assays 26
2.14 Laser-induced Model of CNV 27
2.14.1 Optical Coherence Tomography (OCT) 28
2.14.2 Fluorescein Angiography 28
2.14.3 Tissue Preparation and Immunohistochemistry 28
2.15 Statistical Analysis 29
Chapter III: Results and Discussion 31
3.1 Photophysical Characterization 33
3.2 Manufacture and Characterization of Exosomal $ZnTPPF_{16}(SGal)_4$ 34
3.3 Cellular Uptake of Free $ZnTPPF_{16}(SGal)_4$ by ARPE-19 Cells 39
3.4 Toxicity of Free $ZnTPPF_{16}(SGal)_4$ in ARPE-19 Cells in Dark Conditions and after Light Irradiation 40
3.5 Cellular Uptake of Free vs Exosomal $ZnTPPF_{16}(SGal)_4$ by ARPE-19 Cells 42
3.6 Toxicity of Free vs Exosomal $ZnTPPF_{16}(SGal)_4$ in ARPE-19 Cells in Dark Conditions and after Light Irradiation 43
3.7 Laser-induced Choroidal Neovascularization leads to Retinal Lesions 45
3.7.1 Immunophenotype of Subretinal Lesions 46
Chapter IV: Conclusion and Future Perspectives 49
References 53

Abbreviations

O_2 – Molecular Oxygen
$^1O_2$ – Singlet Oxygen
$(O_2^-)^*$ – Superoxide Anion
AMD – Age-related Macular Degeneration
BCA – Bicinchoninic Acid
bFGF – Basic Fibroblast Growth Factor
BSA – Bovine Serum Albumin
CNV – Choroidal Neovascularization
CRD – Carbohydrate Recognition Domain
DMEM – Dulbecco's Modified Eagle's Medium
DMSO – Dimethyl Sulfoxide
EMT – Epithelial-Mesenchymal Transition
EVs – Extracellular Vesicles
FDA – Food and Drug Administration
FBS – Fetal Bovine Serum
GA – Geographic Atrophy
Gal – Galectin
Hp – Hematoporphyrin
HpD – Hematoporphyrin Derivative
IgG1 – Immunoglobulin G1
LED – Light-emitting Diode
MTT – 3-[4,5-dimethylthiazol-2-yl]-2,5-diphenyltetrazolium bromide
NTA – Nanoparticle Tracking Analysis
OCT – Optical Coherence Tomography
PBS – Phosphate Buffered Saline
PDT – Photodynamic Therapy
PFA – Paraformaldehyde
PS – Photosensitizer
RGC – Retinal Ganglion Cells
ROS – Reactive Oxygen Species
RPE – Retinal Pigment Epithelium
SDS – Sodium Dodecyl Sulfate
VEGF – Vascular Endothelial Growth Factor
TEM – Transmission Electron Microscopy
TGF-β – Transforming Growth Factor Beta
αSma – Alpha-Smooth Muscle Actin

Abstract

Age-related Macular Degeneration (AMD), the leading cause for visual impairment in the elder population (over 55 years old) of developed countries, is a degenerative disease of the macula, the central area of the retina, that causes central vision loss. It is initially characterized by an accumulation of extracellular deposits, called drusen, between the retinal pigment epithelium (RPE) and Bruch's membrane. Over time, AMD can evolve to one of two known advanced states, usually described as dry and wet AMD. The former is often named geographic atrophy (GA) and is characterized by the appearance of atrophic areas in the retina. The latter can be identified by the formation of new choroidal vessels, the cause of many associated problems, including the formation of subretinal fibrosis, responsible for the destruction of retinal cells. Currently, AMD has no cure and just a few treatments can be used to slow the progression of the disease. In fact, the only type of treatable AMD is wet AMD, and the choices revolve around laser photocoagulation (almost obsolete), anti-vascular endothelial growth factor (VEGF) therapy, and photodynamic therapy (PDT) (currently, not used in AMD). Anti-VEGF therapy is the most used and effective treatment in wet AMD, stopping the formation of new vessels from choroid, however, this treatment is not effective for subretinal fibrosis.

PDT is a therapy based on three non-toxic components: a photosensitizer (PS), molecular oxygen (O_2), and a light source with adequate wavelength (dependent on the PS). It has been used in combination with anti-VEGF therapy for wet AMD treatment. Moreover, previous studies have utilized PDT for fibrosis treatment in skin scars and glaucoma.

Based on exosome's intrinsic ability of cell-to-cell communication, the encapsulation of a PS (a galacto-PS, $ZnTPPF_{16}(SGal)_4$), with recognition for the diseased tissue, in exosomes could offer an innovative approach for delivering the payload to the fibrous tissue and new capillaries of the choroid in the case of AMD. In this work, we present a drug delivery system composed by a zinc-porphyrin conjugated with four thiogalactose molecules, $ZnTPPF_{16}(SGal)_4$, and exosomes, to act as drug carriers, as a potential alternative for PDT treatment of fibrosis in wet AMD patients. This galactose-PS was designed for a specific target, namely galactose-binding proteins, galectins that are overexpressed in subretinal fibrosis and choroidal neovascularization (CNV) in AMD. Exosomes obtained from porcine eyecups were used to load the PS. Exosomal $ZnTPPF_{16}(SGal)_4$ has been purified and the loading was evaluated by transmission electron microscopy (TEM) and fluorescence. In the sonication bath, $ZnTPPF_{16}(SGal)_4$ encapsulation/association with exosomes was more successful than in the probe sonication. We have assessed the photophysical properties of the PS and its photodynamic potential in ARPE-19 cell line (with morphology reminiscent of fibroblasts) was compared with exosomal $ZnTPPF_{16}(SGal)_4$. Free and exosomal $ZnTPPF_{16}(SGal)_4$ were found to be incorporated by ARPE-19 cells in a concentration and time-dependent manner. Both were non-toxic until activation by light. PDT-induced cytotoxicity was not significantly different when comparing free $ZnTPPF_{16}(SGal)_4$ and exosomal $ZnTPPF_{16}(SGal)_4$ incubation.

We also aimed to establish a CNV induction model by laser photocoagulation in mice. Based on previous studies, we used a green laser at 532 nm to rupture the Bruch's membrane of wild-type C57BL/6J mice, thus inducing CNV. Results showed we were able to establish the CNV model, in which cells adjacent to the normal RPE monolayer were positive to α-SMA and Ki67, suggesting fibrosis development in this model.

We have shown that after photoactivation, $ZnTPPF_{16}(SGal)_4$ showed high efficacy in inducing ARPE-19 toxicity. The lack of enhancement of photodynamic effect

with exosomal $ZnTPPF_{16}(SGal)_4$ may be related to the source of exosomes, as demonstrated by its lower accumulation in these cells. The presence of CNV and associated fibrotic tissue in the CNV mice model will allow shortly to test the efficacy of PDT for subretinal fibrosis and CNV in AMD.

Resumo

A degenerescência macular da idade (DMI), a principal causa de deficiência visual na população idosa (acima de 55 anos) de países desenvolvidos, é uma doença degenerativa da mácula, a área central da retina, que causa perda de visão central. É inicialmente caracterizado por uma acumulação de depósitos extracelulares, chamados drusa, entre o epitélio pigmentado da retina (EPR) e a membrana de Bruch. Com o tempo, a DMI pode evoluir para um de dois estados avançados conhecidos, geralmente descritos como DMI seca e exsudativa. O primeiro é frequentemente chamada de atrofia geográfica (AG) e é caracterizada pelo aparecimento de áreas atróficas na retina. Este último pode ser identificado pela formação de novos vasos da coroide, a causa de muitos problemas associados, incluindo a formação de fibrose sub-retiniana, responsável pela destruição das células retinianas. Atualmente, a DMI não tem cura e apenas alguns tratamentos podem ser usados para retardar a progressão da doença. Na verdade, o único tipo de DMI tratável é a DMI exsudativa, e as escolhas giram em torno da fotocoagulação a laser (quase obsoleta), da terapia anti-fator de crescimento endotelial vascular (VEGF) e terapia fotodinâmica (PDT) (atualmente, não é usada na DMI). A terapia anti-VEGF é o tratamento mais utilizado e eficaz na DMI exsudativa, impedindo a formação de novos vasos da coroide, no entanto, o tratamento não é eficaz para fibrose sub-retiniana.

A PDT é uma terapia baseada em três componentes não tóxicos: um fotossensibilizador (PS), oxigénio molecular (O_2) e uma fonte de luz com comprimento de onda adequado (dependente do PS). Para o tratamento de DMI exsudativa, tem sido utilizada em combinação com terapia anti-VEGF. Além disso, estudos anteriores já recorreram à PDT para o tratamento de fibrose em cicatrizes da pele e glaucoma.

Com base na capacidade intrínseca do exossoma na comunicação célula a célula, a encapsulação de um PS (um galacto-PS, $ZnTPPF_{16}(SGal)_4$), capaz de reconhecer o tecido doente, em exossomas poderia oferecer uma abordagem inovadora para a entrega do PS ao tecido fibroso e aos novos capilares da coroide presentes num caso de DMI. Neste trabalho, apresentamos um sistema de entrega de fármacos composto por uma zinco-porfirina conjugada com quatro moléculas de tiogalactose, $ZnTPPF_{16}(SGal)_4$, e exossomas, para atuar como veículo de fármacos, como uma potencial alternativa para o tratamento de fibrose em pacientes com DMI exsudativa. Este galactose-PS foi projetado para um alvo específico, nomeadamente proteínas com afinidade à galactose, galectinas, que são sobreexpressas na fibrose sub-retiniana e neovascularização coroideia (CNV) na DMI. Exossomas obtidos de olhos de suíno foram usados para veicular o PS. O $ZnTPPF_{16}(SGal)_4$ exossómico foi purificado e o seu conteúdo foi avaliado por microscopia eletrónica de transmissão (TEM) e fluorescência. A encapsulação/associação de $ZnTPPF_{16}(SGal)_4$ com exossomas usando banho de sonicação foi mais bem-sucedida do que recorrendo à sonicação com sonda. Foram avaliadas as propriedades fotofísicas do PS e seu potencial fotodinâmico na linhagem celular ARPE-19 (com morfologia reminiscente de fibroblastos) foi comparado com o do $ZnTPPF_{16}(SGal)_4$ exossómico. $ZnTPPF_{16}(SGal)_4$ livre e exossómico foi incorporado pelas células ARPE-19 em função da concentração de PS e do tempo utilizados. Ambos se revelaram não tóxicos até a ativação pela luz. A citotoxicidade induzida por PDT não foi significativamente diferente quando se comparou a administração de $ZnTPPF_{16}(SGal)_4$ livre com a de $ZnTPPF_{16}(SGal)_4$ exossómico. Outro dos objetivos deste trabalho passou por estabelecer um modelo de indução de CNV por fotocoagulação a laser em ratinhos. Com base em estudos anteriores, usámos um laser verde a 532 nm para romper a membrana de Bruch de ratinhos C57BL/6J do tipo selvagem, induzindo assim a CNV. Os resultados mostraram que fomos capazes de estabelecer o modelo CNV, no qual as células

adjacentes à monocamada RPE normal foram positivas para α-SMA e Ki67, sugerindo o desenvolvimento de fibrose neste modelo.

Aqui demonstrámos que, após fotoativação, o $ZnTPPF_{16}(SGal)_4$ apresentou alta eficácia na indução de toxicidade em ARPE-19. A ausência de um aumento do efeito fotodinâmico esperado para o $ZnTPPF_{16}(SGal)_4$ exossómico pode estar relacionada com a origem dos exossomas, conforme demonstrado pela sua menor acumulação nessas células. A presença de CNV e tecido fibrótico, associada ao modelo de CNV em ratinhos, permitirá em breve testar a eficácia da PDT para fibrose sub-retiniana e CNV na DMI.

Chapter I

Introduction

1.1 The Human Eye

"Vision is the most important sense of human beings. It is estimated that ~90% external information was collected by the vision system in humans" (Shang, 2017, p. 247). The eye, the fundamental organ for vision, comprises a set of different structures, some of them presented in Fig. 1.1, each with its own function. Light is focused onto the retina by the cornea and lens, which are transparent structures. The retina detects light and turns it into electrical signals, which are then transmitted to the brain via the optic nerve, where they are processed and interpreted by the human brain and translated to images, with a variety of shapes and colors, constituting the ability of sight (Shang, 2017).

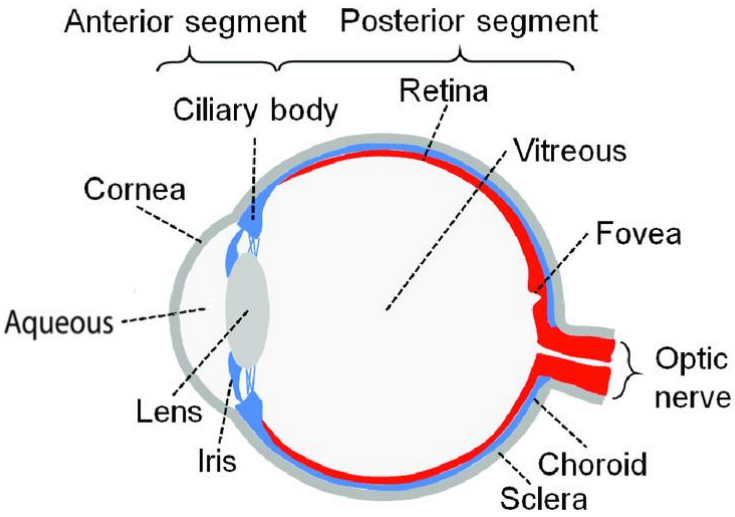

Figure 1.1. Diagram of the human eye. *Adapted from (Chuang, Fields, & Priore, 2017)*.

In order to have a better understanding of how humans are able to see, we need to analyze the human eye. This organ is divided in two segments, anterior and posterior (Chuang, Fields, & Priore, 2017), and even though the second one is of greater interest for this study, both are very important for a normal vision and require characterization, as follows.

1.1.1 Anterior Segment

As illustrated in Fig. 1.1, the anterior segment, the part of the human eye closest to the surface of the eyeball, is composed of the cornea, the lens, the iris, and the ciliary body. Besides these structures, there is also aqueous humor, a liquid flowing in from the ciliary body with plasma-like composition (with less protein and glucose, but more lactic and ascorbic acids) in charge of providing nutrients to avascular structures, remove some of their waste, and keep the intraocular pressure necessary for a proper shaped eye, filling the space between the cornea and both the lens and the iris and even the space surrounding the lens (Gamm & Albert, 2007).

Firstly, regarding the cornea, this being a superficial, transparent, and avascular tissue, it represents the first layer of protection, both to light, by focusing it to the retina

and avoiding scattering, and external agents of infection, like viruses or bacteria (Miesfeld & Brown, 2019; Sridhar, 2018). With these purposes, the cornea consists of six tiers of tissue: three cellular (the corneal epithelium, the stroma, and the endothelium) and three membranous (the epithelial basement, the Bowman's, and the Descemet's membranes). The cellular layers confer structural integrity, health and function when fully developed (Miesfeld & Brown, 2019). On the other hand, Bowman' membrane is helpful in maintaining the shape of the cornea, Descemet's membrane consists of a supporting layer for endothelial cells (Sridhar, Anatomy of cornea and ocular surface, 2018), and the epithelial basement membrane is responsible for anchoring the epithelial cells to the stroma and also to scaffold the embryonic development of these, as well as their processes of migration, differentiation and maintenance of the epithelial phenotype (Torricelli, Singh, Santhiago, & Wilson, 2013).

Regarding the lens, it is important to know that it acts as the second refractive surface of the eye, converging incident light rays to the retina, according to the position of their source, thus enabling the visualization of objects at different distances, in a process called accommodation (Miesfeld & Brown, 2019).

Moving on to the iris and the ciliary bodies, two structures connected by the iris root, it has been described the first one is in charge of controlling intraocular pressure, originated by the circulation of aqueous humor, regulating the amount of photons passing through to the retina, and help focusing nearby objects on the lens; the second is responsible for secreting the previously mentioned aqueous humor, glycoproteins, antioxidant enzymes, and neuropeptides, as well as handling lens accommodation, with the contraction of the ciliary muscles (Miesfeld & Brown, 2019).

1.1.2 Posterior Segment

The posterior segment, as shown in Fig. 1.1, which constitutes the inner part of the ocular globe, is divided in the sclera, optic nerve, choroid, and retina (with a special region called the fovea). It is also worth noting the presence of the vitreous humor, a fragile and transparent hydrogel composed almost exclusively of water, with small traces of type II collagen and hyaluronic acid, involved in the eye's growth during development and its protection against impact (especially the lens and the retina), in the interior of this segment, between the lens and the retina (Tram & Swindle-Reilly, 2018). The sclera, known as the outermost layer of the eye (along with the cornea), is a white and opaque structure, a result of its irregularly arranged collagen fibers, that aims to protect, support, and anchorage the eye as a whole, as well as maintain the shape of the globe (Armstrong & Cubbidge, 2019).

Then, there is the optic nerve, a structure that is estimated to be constituted by "38% of all the axons entering and leaving the central nervous system, that is why humans have such a highly developed visual system (Selhorst & Chen, 2009). Anatomically, it is the result of the aggregation of nearly 1.2 million retinal ganglion cells (RGC), merging from the lamina cribrosa (a three-dimensional network of trabeculae that provides structural and nutrient support to the RGC (Downs & Girkin, 2016)) to the optic papilla and forming the optic nerve, that can be divided into four compartments: intraocular, intraorbital, intracanalicular, and intracranial (Selhorst & Chen, 2009). With the ability to carry action potentials (generated by the retinal photoreceptors), the optic nerve enables the transfer of visual information from the retina to the brain by electrical impulses (Healthline Editorial Team, 2018).

Another very important part of the posterior segment is the choroid, an extremely vascularized, thin, and variably pigmented tissue, located between the sclera and the retina. The choroid is the result of three distinct layers, the choriocapillaris, the stroma, and the lamina fusca. The first one, the so-called choriocapillaris, is responsible for providing nutrients to the RPE and the outer part of the retina. As for the stroma, since it contains dendritic melanocytes (along with fibroblasts and mast cells), conferring it a dark color, it absorbs light that does not reach the retina, thus avoiding light scattering inside the eye. Last, but not least, the lamina fusca, separating the choroid and the sclera, is composed of flattened fusiform melanocytes and fibroblast-like cells, with some bundles of myelinated axons in the middle. The functions of these fibroblast-like cells are to synthesize and secrete extracellular matrix components, namely elastin, collagens, and proteoglycans (Zeiss, Tu, & Treuting, 2017; Armstrong & Cubbidge, 2019). Apart from the functions already described above, the choroid has a role in the thermoregulation of the eye, the adjustment of the position of the retina by changing its thickness, and the secretion of growth factors (Nickla & Wallman, 2009).

Separating the choroid's choriocapillaris and the retina, there is a thin, acellular layer called Bruch's membrane. This membrane, with a composition mostly synthesized by the RPE and the choroid, acts as an attachment site for RPE cells and allows the selective passage of nutrients, from the choroidal vasculature to the retina, and metabolic wastes, from the retina to the circulation (Kwon & Yoo, 2017).

1.1.2.1 Retina

Since the retina is of greater interest for this study, it is only natural that a more detailed explanation is given about this eye structure. The retina is the light-sensitive part of the eye, being able to convert light stimuli into action potentials, that then pass to the brain via the visual pathway (Armstrong & Cubbidge, 2019).

In the outer part of the retina, we can find the RPE, the most posterior part of the retina, characterized as a monolayer of pigmented cells, which has an apical surface with microvilli that connect the RPE with the photoreceptors' outer segments. These outer segments are constantly shed by the photoreceptors, and then phagocyted and degraded by the RPE, ending up on its basal surface, which abuts the choroidal vasculature. Aside from waste removal, the RPE also supplies nutrients and metabolites to the neural retina (RGC, amacrine cells, bipolar cells, horizontal cells, cones, rods, and Müller cells). The RPE monolayer stands between the neuroretina and the choroid, constituting the outer retinal-blood barrier (Miesfeld & Brown, 2019; Armstrong & Cubbidge, 2019).

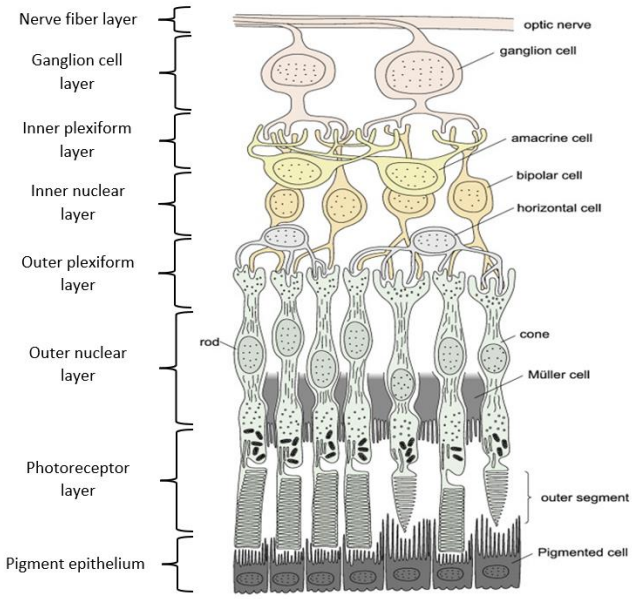

Figure 1.2. Detailed view of the retina. *Adapted from (Imamoto & Shichida, 2014).*

It is important to describe the specialized light-sensitive cells present in the retina, which support vision. These are called photoreceptors, and they can be separated into two types, rods and cones. The rods are responsible for our eyesight in dim light or night vision, in a process involving a photosensitive pigment called rhodopsin, present in this type of cells, as well as numerous mitochondria, a nucleus area, and unique synaptic structures. When photoactivated, rhodopsin causes a chemical cascade reaction, that results in the conversion of light energy into electrical energy. Since rods can only sense the intensity of light, but not its wavelength, they can only represent black and white images. Regarding cones, these are much less numerous than rods, even though they enable color detection, by the photoactivation of a set of different opsins (pigments). On this matter, much like a pixelated screen (television, computer, …), there are three types of cones, sensitive to the colors red, blue, and green, whose interaction allows the production of all colors of the visible spectrum (Armstrong & Cubbidge, 2019; Imamoto & Shichida, 2014).

Both the cornea and the lens focus incoming light rays onto the retina, as previously described. The point of focus is in the central part of the retina, called macula lutea, and especially its center, denominated fovea centralis. The reason behind this is that the macula lutea is composed almost entirely of cones, particularly in the fovea centralis, which is exclusively made of cones. Visual acuity, or the ability to distinguish different colors in detail, is influenced by the density of these photoreceptors, and the higher it is, the more detailed human eyesight will be (Armstrong & Cubbidge, 2019).

As it can be seen in Fig. 1.2, the retina is also composed by retinal ganglion, bipolar, amacrine, horizontal, and glial cells (Müller cells, astrocytes, and microglia), each with a distinct role to perform in the creation and transmission of vision. RGC represent the main neuron output of the retina and simultaneously constitute another light-sensitive type of cells, crucial in melatonin release modulation and pupil size regulation. Regarding bipolar cells, classified as neurons, these are in charge of receiving visual inputs from photoreceptors and projecting their axons onto RGC (Mahabadi & Khalili, 2021). As for horizontal and amacrine cells, two types of retinal interneurons, these are

responsible for the modulation of information flow in the retina. Specifically, horizontal cells modulate information from photoreceptors to bipolar cells in the outer plexiform layer, and amacrine cells do the same from bipolar cells to RGC in the inner plexiform layer. As for glial cells, they constitute about half the cells of the central nervous system and participate in almost every part of its formation and function (Allen & Lyons, 2018). The primary type of glial cells found in the retina are Müller cells. Müller cells play a significant role in the maintenance of the function and health of the retina. Since it is the only cell type that spans across the entire retina, Müller cells are particularly important for retinal homeostasis. In healthy conditions, Müller cells are responsible for recycling neurotransmitters, preventing glutamate toxicity, redistributing ions by spatial buffering, participating in the retinoid cycle, and regulating nutrient supplies. Any loss of function in these cells will affect the entire retina (Coughlin, Feenstra, & Mohr, 2017). Astrocytes (or astroglial cells) are almost exclusively restricted to the innermost retinal layers. They are believed to be originated in the optic nerve, migrate from it, and enter the retina with its blood vessels. Astroglial cells are deeply involved in retinal neovascularization, as the main producers of VEGF. Other roles played by astrocytes are neurotrophic support, enhanced mechanical aid for degenerating axons, and maintenance of the blood-retina barrier (Vecino, Rodriguez, Ruzafa, Pereiro, & Sharma, 2016). Microglia consist of tissue macrophages that represent the innate immune system of the central nervous system. It is believed that microglia originates from mesodermal elements that penetrate nervous tissue during embryonic and fetal stages, and becomes fully established during postnatal life. Its main function is to create a protective environment within the central nervous system, by scanning the brain and searching for signs of brain damage. In case of a neural injury, microglia shows morphological changes characterized as its "activation" (Cardona, Ransohoff, & Akassoglou, 2013).

1.2 Age-Related Macular Degeneration (AMD)

1.2.1 Pathology

AMD is a chronic and progressive disease that affects the retina, more specifically, its central area, the macula lutea (described in 1.1.3), resulting in central vision loss. This retinal disease is initially characterized by an accumulation of extracellular deposits of lipoproteins and inflammatory constituents (Gelfand & Ambati, 2016), called drusen, between the RPE and Bruch's membrane (Zhang & Sivaprasad, 2021). Loss of photoreceptors can also occur in the early/intermediate stages of the disease (Fleckenstein, et al., 2021). AMD is also linked to chronic inflammation, lipid deposition, oxidative stress, or abnormalities of extracellular matrix turnover (Fleckenstein, et al., 2021).

AMD is classified as early or intermediate based on the size, position, and quantity of drusen, as well as the presence of pigmentary alterations (a marker of RPE illness) (Gelfand & Ambati, 2016). AMD can progress to one of two types of advanced/late stages: dry or GA and wet or exudative.

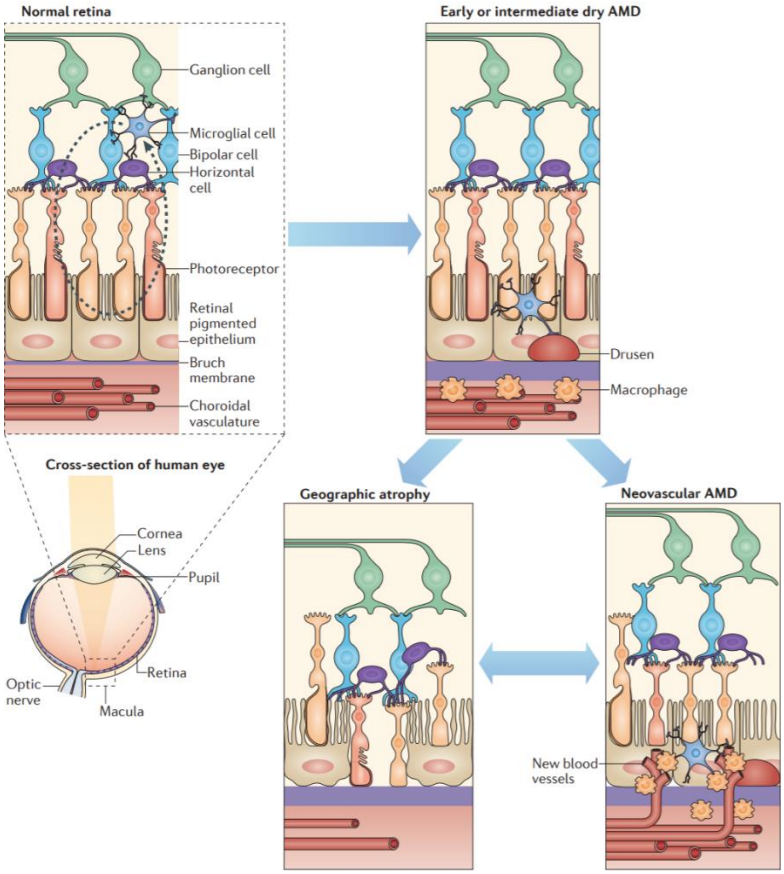

Figure 1.2. Retinal anatomy in the different AMD stages *(Ambati, Atkinson, & Gelfand, 2013).*

Firstly, dry AMD, also identifiable as GA, consists of a progressive deterioration of the RPE, the photoreceptor layer, and the choroidal capillaries in the macula (Ruan, Jiang, & Gericke, 2021). This process results from the accumulation of drusen, generating areas of atrophy that become more and more confluent with time, causing vision loss (Yonekawa, Miller, & Kim, 2015).

Secondly, wet AMD, commonly described as neovascular or exudative AMD, is characterized by the formation of new choroidal vessels. These newly formed vessels tend to invade the retina, breaking through the Bruch's membrane and causing fluid exudation, retinal hemorrhages, and possibly detachment of the RPE or the retina. This form of AMD causes vision loss to occur quicker than GA (Ruan, Jiang, & Gericke, 2021).

Lastly, since it constitutes the focus of this work, it is important to highlight subretinal fibrosis, a prevalent issue in neovascular AMD patients. The formation of subretinal fibrosis can result in the local destruction of the RPE, photoreceptors, and even choroidal vessels, inducing permanent dysfunction of the macula and consequent vision loss. Subretinal fibrosis is thought to be a wound healing response to the tissue damage caused by CNV. The formation of this type of fibrosis shares molecular mechanisms with fibrosis in other organs, which means that, shortly after tissue injury, epithelial cells release mediators that recruit, amongst other types of cells, fibroblasts (Ishikawa, Kannan, & Hinton, 2015). Another source of fibrosis formation is the epithelial-mesenchymal transition (EMT) that cells undergo, consisting of a conversion of epithelial cells to myofibroblasts. Aside from these natural processes of fibrosis formation, anti-VEGF

therapy (described in 1.2.4.3), the most common treatment for CNV, can also induce fibrosis formation, a consequence of the frequent intravitreal injections associated with this treatment (Ishikawa, Kannan, & Hinton, 2015). In fact, a study showed that half of the eyes treated with anti-VEGF therapy for a 2-year period developed scar tissue (Daniel, et al., 2014).

1.2.2 Prevalence and Risk Factors

AMD is the leading cause of vision impairment in the elder population, particularly for those over the age of 55, of developed countries. Currently, the global prevalence of AMD is estimated at around 196 million cases (Tan, Zou, Yoshida, Jiang, & Zhou, 2020). For any form of AMD between the age of 45 and 85 years is approximately 8.7%, even though it varies substantially among races and ethnicities (Ricci, et al., 2020). For example, metanalysis results of AMD prevalence in 129664 subjects, with 12727 cases from 39 studies, showed a range from 7.3% in Asian populations to 12.3% in European ancestry populations (Wong, et al., 2014). These significant variations in prevalence can be attributed to genetic, lifestyle, and/or diet differences (Ricci, et al., 2020).

In addition, for people 70 years old or older, the prevalence of early and late AMD was found to be 13.2% and 3.0%, respectively. These were the results of a study that encompassed 42080 subjects from ten European countries (Colijn, et al., 2017). At the same time, it is important to refer that, even though dry AMD accounts for most AMD cases (80 to 85%), wet AMD is responsible for approximately 80% of severe vision loss cases (Thomas, Mirza, & Gill, 2021).

Moreover, due to the increase in life expectancy, it is fair to assume AMD prevalence will rise in years to come. Metanalysis estimates the number of AMD patients worldwide to reach 288 million by 2040 (Ricci, et al., 2020).

Regarding risk factors, the most relevant for any stage of AMD is age. With aging, the accumulation of oxidative damage associated with it is believed to be the primary trigger of age-related degenerative diseases (Tan, Zou, Yoshida, Jiang, & Zhou, 2020). Another well-established risk factor is ethnicity, as results revealed significantly higher values of AMD prevalence for Europeans and North Americans when compared to Asians, Africans, and Hispanics (Wong, et al., 2014). Other risk factors include lifestyle (smoking, sleep patterns, obesity, light exposure, amongst others), dietary habits, and some systemic diseases (such as hypertension, diabetes mellitus, or cardiovascular diseases) as determining factors for the development of a specific type of AMD, depending on the risk factor in question (Singh, et al., 2017).

1.2.3 Galectins in Wet AMD

Galectins (Gal) constitute a family of proteins with high affinity to carbohydrates, particularly β-galactose residues. The binding of Gal with these molecules is mediated by a carbohydrate recognition domain (CRD), composed of 130 amino acids, present in all Gal types. Until today, 15 different types of Gal have been identified in mammals (only 11 in humans). These can be categorized according to their structure, dividing them into three groups: prototypical Gal, namely Gal1, Gal2, Gal5, Gal7, Gal10, Gal11, Gal13, Gal14, and Gal15, distinguishable by their single CRD, with the ability to act as monomers or form homodimers; the chimeric Gal3 (a group by itself), composed of a

single CRD and a large amino-terminal domain, easing the formation of oligomers; tandem repeat Gal, which includes Gal4, Gal6, Gal8, Gal9, and Gal12, formed by two CRDs, connected through a small peptide domain (Manero-Rupérez, Martínez-Bosch, Barranco, Visa, & Navarro, 2020).

In the cases of Gal1, Gal3 and Gal9, these are expressed across a variety of tissues, such as immune, endothelial, and epithelial cells, as well as sensory neurons. On the other hand, other Gal are found in specific tissues and localizations, like the cases of Gal7, commonly found in the skin, Gal 12, abundant in adipose tissues, or even Gal5, only discovered on rat reticulocytes (Bacigalupo, Manzi, Rabinovich, & Troncoso, 2013).

In general, Gal take part in several cellular and intercellular mechanisms, for binding to endogenous glycans. Biologically, Gal play roles in development, tissue regeneration, regulation of immune cell activities (inflammatory responses and immune system) among other cellular functions (Hara, et al., 2020). In addition, different members of the Gal family are able to monitor the endosomal or lysosomal membrane by binding with β-galactose present in glycoconjugates exposed after membrane damage (Banfer & Jacob, 2020).

Specifically, Gal-1 has already been proved to take responsibilities in cell growth, migration, and proliferation. Moreover, Gal1 was found to facilitate angiogenesis and fibrosis by altering the signaling pathways of the receptors of VEGF-A and transforming growth factor beta (TGF-β), known angiogenic and fibrogenic factors, respectively. In wet AMD, a laser-induced CNV and subretinal fibrosis model developed by Wu in 2019 (Wu, et al., 2019), proved the involvement of Gal1 in CNV and subretinal fibrosis (mediated via EMT).

As for Gal-3, it constitutes an active part in cell-to-cell or cell-to-matrix interactions, cell growth, cell differentiation, macrophage activation, antimicrobial activity, angiogenesis, fibrosis, and apoptosis (Hara, et al., 2020). The discovery of the important role played by Gal3 in VEGF and basic fibroblast growth factor- (bFGF) mediation for angiogenic response raised interest on if it may be part of the pathogenesis of wet AMD. Other studies reported elevated levels of Gal 3 in advanced dry AMD (Argueso & Panjwani, 2011).

1.2.4 Current Therapies

1.2.4.1 Early and Intermediate AMD

As of today, there are no therapies available for early or intermediate AMD. In fact, the only strategy available is to try to prevent it from worsening. In this regard, lifestyle changes such as quitting smoking, wearing coated lenses to protect the eyes from ultraviolet A and B radiation, and increasing antioxidants intake and supplementation in diet can help slow down oxidative stress, which is one of the causes of tissue degeneration in early and intermediate AMD (Kniggendorf, Dreyfuss, & Regatieri, 2020).

Specifically for intermediate AMD, results from AREDS 2 (Age-Related Eye Disease Study 2), developed by the Age-Related Eye Disease Study 2 Research Group (AREDS 2 Research Group, 2014), demonstrated that vitamin supplementation can reduce disease progression for 25% of the patients and the risk of vision loss within five years by 19% (Kniggendorf, Dreyfuss, & Regatieri, 2020).

1.2.4.2 Dry AMD

Currently, dry AMD lacks treatment, so, just as early and intermediate AMD, preventing its progression is the only course of action for patients. As described in 1.2.4.1 for intermediate AMD, AREDS 2 revealed vitamin supplementation can also be helpful in dry AMD cases (Kniggendorf, Dreyfuss, & Regatieri, 2020).

As for future therapies, several studies are presently in progress. Based on the work of Donoso (Donoso, Vrabec, & Kuivaniemi, 2010), that identified degeneration mechanisms as pathogenic pathways of dry AMD, particularly those involving complement factor H, interfering with these pathways has become of interest as a therapeutic strategy. In that regard, preclinical studies on this and other complement factors are in current development. Another area of focus has been cell therapy, particularly clinical trials of cell transplantation on patients with severe vision loss associated with GA. The use of stem cells to try to repair the RPE (Song, et al., 2015) and the use of induced pluripotent stem cells engineered to function and express photoreceptor features are two examples of cell therapy (Garcia, et al., 2015).

1.2.4.3 Wet AMD

Contrarily to dry AMD, patients suffering from wet AMD have many treatment alternatives. Interestingly enough, the first paper published about wet AMD treatment dates back to 1982, when a research group revealed the results from a therapy called Laser Photocoagulation (Macular Photocoagulation Study Group, 1982). This technique used an Argon laser to coagulate new choroidal vessels but has since become obsolete due to its side effects, registered in a study conducted by the same group in 1994 (Macular Photocoagulation Study Group, 1994). Soon after, in 1999, the Food and Drug Administration (FDA) approved the first PS, Verteporfin (Visudyne^{TM}; Novartis Ophthalmics, Basel, Switzerland), for PDT in AMD (described in 1.3.1). This therapeutic approach involves the intravenous administration of a photosensitive molecule which, when activated by light of a specific wavelength, reacts with O_2 in target tissues to produce reactive oxygen species (ROS), that cause cell death (Kwiatkowski, et al., 2018). At the time, this new treatment had success in slowing the rate of vision loss, but visual stabilization or improvement were rarely seen (Khanna, et al., 2019). In the early 2000s, a new type of treatment came to fruition, anti-VEGF therapy, which consisted of periodical injections. This solution was developed due to the critical role of VEGF (a group of proteins that includes VEGF-A, VEGF-B, VEGF-C, VEGF-D, and VEGF-E, along with placental growth factor) in angiogenesis and vascular permeability. The first anti-VEGF agent approved by the FDA was pegaptanib sodium (Macugen; Eyetech Pharmaceuticals, New York, New York), in 2004, since fallen out of favor (Khanna, et al., 2019).

Nowadays, almost all wet AMD treatments are made by anti-VEGF therapy, the reason being that this type of treatment shows stabilization and improvement of visual acuity, by preventing the bond between VEGF and its endothelial cell receptor. The most common anti-VEGF agents for clinical use today are Ranibizumab (Lucentis; Genentech, Inc., San Francisco, California), Bevacizumab (Avastin; Genentech, Inc., San Francisco, California), and Aflibercept (EYLIA; Regeneron Pharmaceuticals, Inc., Tarrytown, New York) (Kniggendorf, Dreyfuss, & Regatieri, 2020).

Ranibizumab, a recombinant humanized immunoglobulin G1 (IgG1) kappa monoclonal antibody fragment that binds to all active isoforms of VEGF-A, was

approved for clinical use in wet AMD in June of 2006. Since then, several clinical trials have confirmed the safety and efficacy of intravitreal injections with this anti-VEGF agent. Moreover, treatments with this drug resulted in morphological enhancements of the retina, more specifically, decreases the area of CNV lesions and retinal thickness (Kniggendorf, Dreyfuss, & Regatieri, 2020).

Bevacizumab is another humanized recombinant IgG1 monoclonal antibody that binds to activated VEGF-A, developed by the same company. It differs from ranibizumab because it consists of a complete IgG1 molecule (ranibizumab contains only the antigen-binding fragment of the same antibody). Despite the fact that systemic administration of bevacizumab has been used in the treatment of wet AMD with good results (improved visual acuity and decreased central retinal thickness) in the SANA (drug safety) clinical trial, and several studies have confirmed the safety and efficacy of intravitreal injections with this drug for this disease, bevacizumab has not been approved for intraocular use (Kniggendorf, Dreyfuss, & Regatieri, 2020).

Aflibercept, one of the most recently FDA approved anti-VEGF agent, back in 2011, is characterized as recombinant fusion protein composed by ligand-binding elements of VEGF receptor 1 (VEGFR-1) and VEGFR-2, fused to the human IgG1 Fc segment, able to block all VEGF-A isoforms, VEGF-B, and placental growth factor. This drug stands out from the previous two since its bimonthly administration was proved to have a similar efficacy to a monthly administration of ranibizumab (Yonekawa, Miller, & Kim, 2015). This seems to be the result of higher binding affinity of aflibercept to VEGF-A, VEGF-B and placental growth factor than ranibizumab and bevacizumab (Papadopoulos, et al., 2012).

These anti-VEGF agents demonstrate efficacy in wet AMD, allowing patients to improve or retain visual function. Sometimes, however, patients do not respond to this treatment and continue to lose vision over time, and slowly lose the abilities to read, drive, amongst other daily activities. For these reasons, it is of upmost importance to continue the research of new therapies, new diagnostics, and even new anti-VEGF agents. Some examples of new approaches in current development include the inhibition of nucleoside reverse transcriptase, gene therapy, RNA interference, and epiretinal radiotherapy (Kniggendorf, Dreyfuss, & Regatieri, 2020).

1.3 Photodynamic Therapy (PDT)

1.3.1 Principle of PDT and its Applications

PDT is a non-invasive therapeutic approach that can be employed in a variety of cancers, dermatological (such as actinic keratoses, psoriasis, verruca vulgaris, and others), gynecological and urological conditions. Concerning wet AMD, it was used in combination with anti-VEGF therapy (Kwiatkowski, et al., 2018). Some studies also indicate PDT as a treatment for fibrosis in skin scars (Mendoza-Garcia, Sebastian, Alonso-Rasgado, & Bayat, 2015) and glaucoma (Diestelhorst & Grisanti, 2002).

This type of therapy is based on three non-toxic components: a photosensitizer, O_2, and a light source with adequate wavelength (dependent on the PS) (Kwiatkowski, et al., 2018). The PS is a prodrug sensitive to light at one or more wavelengths, that targets malignant or diseased tissues and accumulates inside them (Dobson, Fernandes de Queiroz, & Golding, 2017). Once inside the cells, the PS is photoactivated with the appropriate light wavelength, coincident with the absorption spectrum of the PS, which

leads the PS to its first excited singlet state. This unstable state can decay by emitting fluorescence or the intersystem crossing process, it can attain the more stable excited triplet state. In its triplet state, the PS can directly react with biomolecules (Type I photochemical reaction) or transfer its energy to O_2 (Type II photochemical reaction) to produce ROS, especially singlet oxygen ($^1O_2$), described in detail below (Kwiatkowski, et al., 2018).

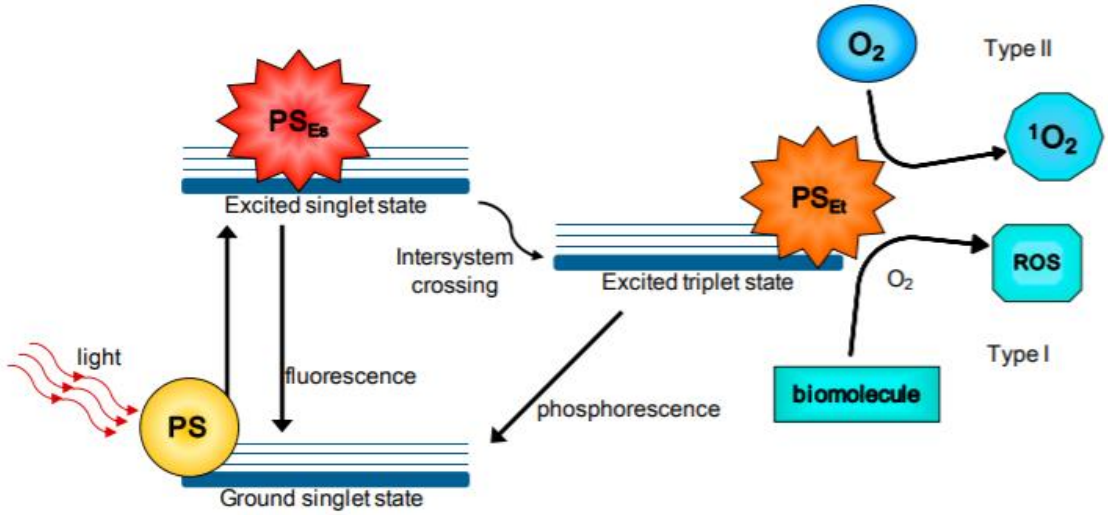

Figure 1.3. - Type I and Type II photochemical reactions in PDT *(Calixto, Bernegossi, de Freitas, Fontana, & Chorilli, 2016)***.**

1.3.1.1 Type I Photochemical Reaction

In type I photochemical reactions, the PS in its excited triplet state (T_1) can transfer energy to surrounding biomolecules, constituents of the targeted area. In this interaction, a hydrogen or an electron are transferred (reduction-oxidation reactions), leading to the formation of free radicals and anion radicals of the PS and the biomolecule, respectively. The electrons originated in this process will then react with O_2, producing ROS (specifically, superoxide anion radicals (O_2^{-*})) inside the target cells. Due to the cytotoxicity of this and of a subsequent generation of ROS, consequent oxidative stress will lead to the destruction of the cells (Kwiatkowski, et al., 2018).

1.3.1.2 Type II Photochemical Reaction

Regarding type II photochemical reactions, the energy involved in the transition of the PS to the excited triplet state passes directly to the O_2 present in the targeted cells. With this energy, O_2, the so-called basic triplet state of O_2, will transition to a singlet state, highly cytotoxic. The result of this process is oxidative stress and consequent cell death (Kwiatkowski, et al., 2018).

Even though there are many factors (oxygen concentration, pH, tissue dielectric constant and the structure of the PS) that influence the ratio of contribution between the

two types of photodynamic reactions, it is believed that type II mechanisms represent a bigger share in the conditioning of PDT efficiency (Kwiatkowski, et al., 2018).

1.3.2 Photosensitizers (PS)

As reported by Daniell and Hill in 1991, the therapeutic use of light goes back to ancient civilizations, namely Egyptians, Chinese, Indians, and Greeks. At the time, it was a treatment for diseases like vitiligo, psoriasis, skin cancer, or even psychosis (Daniell & Hill, 1991). Despite this, it was not until 1841 that the first PS was discovered, when H. Scherer extracted hematoporphyrin (Hp) by removing iron from dried blood. Since then, three different generations of photosensitizers have been developed and used in PDT (Kou, Dou, & Yang, 2017).

The first generation of photosensitizers consisted of Hp, after its derivative HpD was found to possess cancer cell selectivity. Further research led to the creation of photofrin (porfimer sodium, a purified form of HpD) for possible use in cancer treatment (Chau, Xie, & Wong, 2021). Early clinical trials with HpD in PDT for cancer showed some efficiency in several organs (brain, laryngeal, lung, skin, gastric, and esophageal carcinomas) (Kou, Dou, & Yang, 2017). However, after numerous clinical studies, limitations like long clearance time, low chemical purity, and a short excitation wavelength were identified, thus promoting the development of a second generation of PS (Chau, Xie, & Wong, 2021).

Most of the second generation of PS, such as benzoporphyrins, purpurins, texaphyrins, phthalocyanines, naphthalocyanines, and protoporphyrin IX are based on the structure of porphyrins, due to its ability to generate $^1O_2$ (provoking oxidative stress). Other second-generation PS are chlorin-based PS, such as mono-aspartyl chlorin e6, temoporfin, and hexylpyropheophorbide, as well as some specially designed PS, designed for specific clinical applications (e.g., mitochondria-targeting photosensitizers). In comparison with the first generation, this one was characterized by clear compositions and structures of the PS, as well as improvements in photosensitivity, absorption spectrum and tissue selectivity. With time, PDT with second-generation photosensitizers stopped fulfilling the expectations of investigators, hoping for more accurate targeting and, consequently, less phototoxicity in normal tissues, creating the need for a third generation of photosensitizers (Kou, Dou, & Yang, 2017).

Third-generation PS can dramatically improve PDT efficacy against malignant and nonmalignant diseases. Due to their composition and structure, the third-generation photosensitizers can present higher tissue affinity. When combined with drug delivery systems, they can lead to an enhancement of the phototoxic effect in the damaged tissue without affecting neighboring healthy tissues. In this case, eventually, the dosage required for optimal therapeutic effects will be lower. At the moment, gene engineering for PDT mediation (e.g., Babincová, Sourivong, & Babinec, 2000; Shahzidi, et al., 2013; Takehara, et al., 2017) and the use of nanotechnology in PDT (e.g., Ohulchanskyy, et al., 2007; Lima, et al., 2013; Son, et al., 2018) emerge as the two main branches of research for third-generation photosensitizers (Kou, Dou, & Yang, 2017).

1.4 Drug Encapsulation in Extracellular Vesicles

1.4.1 Extracellular Vesicles (EVs)

EVs constitute a group of membrane vesicles, with typical diameters ranging from 50 to 1000 nm, containing different types of RNA (mRNA, miRNA, Inc RNA, lipids, and proteins, secreted by most living cells (Vader, Mol, Pasterkamp, & Schiffelers, 2016). These include microvesicles (bud directly at the plasma membrane), exosomes (derived from multivesicular bodies), and apoptotic bodies (released by the cell upon its death). (Fuhrmann, Serio, Mazo, Nair, & Stevens, 2014).

Recent studies revealed that small-sized EVs, namely exosomes (50-200 nm), play a key role in intercellular communication and in the removal of cellular contents. Exosomes possess certain organotropic behaviors (affinity to particular tissues or organs) as active participants in cell-to-cell communication, and transport and deliver their protein-, lipid- or nucleic acids-cargo to recipient cells. Moreover, exosomes cargo molecules may play a key role in secreting certain factors, eliciting a response in distant cells (Antimisiaris, Mourtas, & Marazioti, 2018).

As previously stated in 1.3.2., new drug delivery systems are in need, particularly those showing higher affinity to diseased tissues. Due to their high and specific affinity to certain organs and participation in intercellular communication, exosomes have been studied as drug carriers with therapeutical applications for the past few years (Antimisiaris, Mourtas, & Marazioti, 2018).

Exosomes can be isolated from cells or biological fluids in a variety of ways. However, it is hard to obtain a purified fraction of exosomes that are totally free of other EVs types. Exosomes can be isolated by ultracentrifugation (most common method, based on the size and density differences of the components present in the sample), immunoaffinity (results from the affinity between antibodies and specific exosome surface proteins), precipitation (enabled by the alteration of the solubility of the exosomes), and a few other methods (Antimisiaris, Mourtas, & Marazioti, 2018).

1.4.2 Drug Loading Methods

On one hand, EVs possess a lipid bilayer membrane that confers protection to its cargo from degradation in the bloodstream, essential in drug administration. On the other hand, this membrane, along with the content already present in EVs, makes drug loading in EVs a challenging process (Vader, Mol, Pasterkamp, & Schiffelers, 2016). Nevertheless, presently, drug loading can be performed in many ways, based on three different approaches: pre-loading, microfluidic, and post-loading methods (Antimisiaris, Mourtas, & Marazioti, 2018).

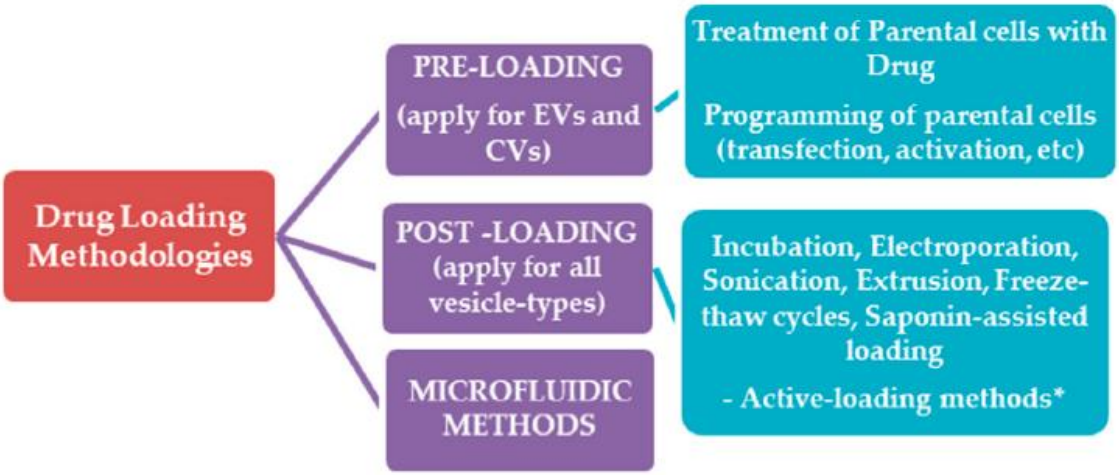

Figure 1.5 Drug Loading Methods *(Antimisiaris, Mourtas, & Marazioti, 2018).*

In pre-loading methods, investigators start by producing (programming of parental cells) or loading (drug treatment of parental cells) the desired drug in parental cells. From these pre-loaded parental cells, extracellular (or cellular) vesicles are then isolated or produced, already containing the drug (Antimisiaris, Mourtas, & Marazioti, 2018).

Microfluidic methods are based on the use of technology to precisely control and manipulate fluids and fluid interfaces at a very small scale. In drug loading, these methods can be applied to the synthesis of exosome-based nanoparticles that act as drug carriers (Yu, Lee, & Lee, 2009).

Regarding post-loading methods, these are characterized by performing drug loading in EVs after their isolation. On that subject, post-loading methods include incubation with the drug, electroporation, extrusion, freeze/thaw cycle method, saponin-assisted loading, and sonication (used in this study) (Antimisiaris, Mourtas, & Marazioti, 2018).

In summary, incubation is a simple mix of EVs with the drug, based on the concentration gradient and consequent passive diffusion; electroporation is characterized by the use of an electric field to increase the EV's membrane permeability, allowing the passage drug access into the EVs; extrusion consists of a mixture of EVs and the drug loaded into a syringe-based lipid extruder, whose extrusion results in membrane disruption, enabling the entrance of the drug into the EVs; freeze/thaw cycle method comprises a mix of EVs with the drug at room temperature, followed by, at least, three cycles of freezing at -80^{o}C and thawing at room temperature, to ease drug encapsulation; saponin-assisted loading uses a surfactant molecule, namely saponin, to originate pores in the membrane of EVs, increasing membrane permeability (Antimisiaris, Mourtas, & Marazioti, 2018).

As for sonication, the post-loading method used in this project, it is characterized by the utilization of sound waves to produce physical vibrations in the solution in study. This can be achieved with a bath sonicator or a probe sonicator (Ghauri, Ghauri, Elhissi, & Ahmed, 2020). For drug loading, EVs are mixed with the desired drug and then sonicated, either by bath or probe sonication, resulting in the deformation of the membrane of EVs and consequently an increase in drug influx into the EVs (Antimisiaris, Mourtas, & Marazioti, 2018).

1.4.3 Applications

At the moment, most studies performed with small EVs as drug delivery systems used exosomes derived from cancer cells, dendritic cells, mesenchymal stem cells, and biological fluids (Antimisiaris, Mourtas, & Marazioti, 2018). Being a novel locus of research, the majority of these projects are proof-of-concept studies, focused on the ability to efficiently load drugs into exosomes, the capability of these exosomes to retain the drug content in in vivo conditions, and the drug delivery potential of these loaded-exosomes, in comparison with the free administration of the drug (Antimisiaris, Mourtas, & Marazioti, 2018).

Nevertheless, pre-clinical studies using exosome-like vesicles as drug delivery systems have already been conducted for a variety of diseases, including several types of cancer (e.g., Munoz, et al., 2013; Ohno, et al., 2013; Ding, et al., 2021), cardiovascular diseases (e.g. Bei, et al., 2017), neurodegenerative diseases, like Alzheimer and Parkinson (e.g., Cunha, Amaral, Sousa Lobo, & Silva, 2016), musculoskeletal diseases (e.g., Bellavia, et al., 2018), and diabetes-related complications (e.g., Yao & Ricardo, 2016). Moreover, some projects have been studying the possibility of small EVs crossing the blood-brain barrier (Antimisiaris, Mourtas, & Marazioti, 2018).

From the preliminary results of early clinical studies, it is clear there are obstacles to overcome in the use of exosome-like vesicles as drug carriers. These barriers include the abundance of starting material and the logistics of the process of exosome-like vesicles production; the drug loading efficiency; the targeting efficiency; the development of scalable methods for drug-loaded exosome manufacturing (Antimisiaris, Mourtas, & Marazioti, 2018).

1.5 Animal Model for CNV Induction

A reproducible animal model for CNV induction was first developed by S. J. Ryan in 1979. By observing the occurrence of subretinal neovascularization after laser therapy in macular lesions, the author postulated that laser therapy itself could induce subretinal neovascularization, through the disruption of Bruch's membrane, and performed an experiment in adult rhesus monkeys. Using an argon laser, inserted in a slit lamp, small-sized eye spots (50 to 100 μm) were irradiated with high-intensity (200 to 900 mW) and short duration (100ms) pulses. Results showed that laser induction led to the development of subretinal neovascularization (Ryan, 1979). This model accurately mimicked CNV present in wet AMD, even though it differed from wet AMD in the origin of these new choroidal vessels, being a wounding model for a symptom initiated by aging changes (Gong, et al., 2015).

Over time, other CNV induction studies have been conducted (e.g., Gong, et al., 2015; Lambert, et al., 2013; Balser, Wolf, Herb, & Langmann, 2019), all based on the work of S. J. Ryan. These studies were performed almost exclusively in mice (mostly C57BL/6J), with the help of several types of laser (e.g. Quantel Medical Vitra^{TM} – Balser et. al, 2019; Alcon Ophthalas 532 EyeLite - Lambert, et al., 2013; green argon laser - Gong, et al., 2015), and laser irradiation was made with distint laser settings, including spot size, power and duration, and different numbers and locations of the laser burns, all successful (in the case of the examples presented) in the induction of CNV, due to the disruption of Bruch's membrane (Gong, et al., 2015).

1.6 Objectives

In this work, we propose an alternative drug delivery system for a PS in PDT as a treatment for CNV and subretinal fibrosis found in wet AMD (as stated in 1.2.1).

The PS consists of a zinc-porphyrin conjugated with four thiogalactose molecules ($ZnTPPF_{16}(SGal)_4$). Due to the aforementioned high affinity of Gal to carbohydrates and their role in angiogenesis and fibrosis (particularly, Gal1 and Gal3), described in 1.2.4, the galactose molecules present in the PS should serve as a diseased tissue targeting booster.

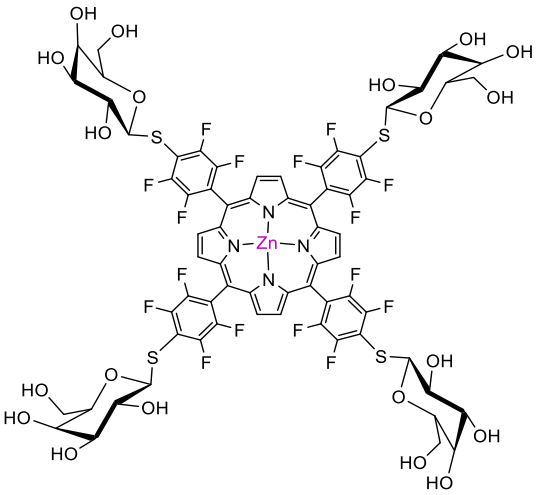

Figure 1.6. – Chemical structure of $ZnTPPF_{16}(SGal)_4$. *Adapted from* (Melo, 2020).

For delivery system, exosomes derived from the RPE were chosen. The use of exosomes is justified by their participation in intercellular communication and the affinity showed to specific tissues (detailed in 1.4.1), since they may also contribute to diseased tissue targeting.

To investigate the use of exosomes as drug carriers of our PS, we will characterize the PS according to absorption spectrum, photostability, and fluorescence to assure this PS has the right physical and chemical properties to be a good therapeutic agent in PDT. After, we will perform drug encapsulation tests, mixing exosomes with our PS and testing post-loading methods to facilitate the entry of the PS into the exosomes. The objective of this part of the work is to find the best method to encapsulate the PS in exosomes and evaluate the efficacy of this process, which required a characterization of the exosomal PS (PS attached/encapsulated in exosomes) regarding fluorescence, particle size, and electrodensity.

In vitro studies will be performed aiming to prove the utility of this PS in PDT for the treatment of subretinal fibrosis in wet AMD. Assessment of cellular uptake and phototoxicity of free PS will be carried out in ARPE-19 cells, an immortalized cell line of RPE with a fibroblast phenotype. After that, we will test the uptake and phototoxicity of exosomal PS against free PS in ARPE-19 cells, with the aim of understanding the therapeutic potential of the PS when delivered by exosomes.

We also intended to establish an animal model of CNV based on laser photocoagulation, and on the works mentioned in 1.5. In this case, we will use a green laser at 532 nm. The main objectives are to assess the best laser settings (namely laser

power, spot size and pulse duration) and spot distributions to be used for the disruption of Bruch's membrane, essential to this wounding response model (explained in 1.5).

The success of this model can be determined by the rupture of Bruch's membrane, the appearance of retinal fluid leakage, and/or the development of CNV (not included in this study) or fibrosis in lesions areas.

Chapter II

Materials and Methods

2.1. Preparation of $ZnTPPF_{16}(SGal)_4$

A zinc porphyrin conjugated with four units of galactose ($ZnTPPF_{16}(SGal)_4$) was provided by Dr. João Tomé team at Centro de Química Estrutural, Chemical Engineering Department, Instituto Superior Técnico, University of Lisbon, Portugal.

A stock solution at 10 mM of $ZnTPPF_{16}(SGal)_4$ was prepared in dimethyl sulfoxide (DMSO), from Sigma-Aldrich®. After solubilization in an ultrasonic bath for 30 min, aliquots were made and stored at -20ºC, in dark conditions. Freshly working solutions were prepared from the stock solution at different conditions, for the different experiments.

2.2 Visible Characterization of $ZnTPPF_{16}(SGal)_4$

Solutions of $ZnTPPF_{16}(SGal)_4$ at the concentrations of 2, 20 and 50 µM were freshly prepared in DMSO, phosphate buffered saline (PBS) with 0.5% DMSO and 1% sodium dodecyl sulfate (SDS) (Sigma-Aldrich®). Then, 100 µL of each solution were added directly to each well in a 96-well plate. The absorption spectra were assessed by measuring the absorbance between 400 nm and 800 nm. PBS was prepared in Milli-Q water and consisted of 137mM of NaCl, 27mM of KCl, 81mM of Na_2HPO_4 and 15mM of KH_2PO_4, pH 7.4 (Sigma-Aldrich®). Visible absorbance was measured using the Synergy™ HT microplate reader from BioTek Instruments®. The data acquisition was performed using the Biotek´s Gen5™ Data Analysis Software.

2.3 Photostability Assay

To assess $ZnTPPF_{16}(SGal)_4$ photostability, the PS was irradiated with white light using a light-emitting diode (LED) array system (with a matrix of 17x11 LEDs) for 40 min. The LED system emits white light with two emission peaks at wavelengths at 450 ± 20 nm and 550 ± 50 nm, with a total fluence rate of 8.4 $mW.cm^{-2}$. This system was energetically supplied by an 800-mA plug-in adaptor from MW. The absorbance readings (Synergy™ HT) at 415 nm for different time points were performed. For this assay, a working solution of 20 µM $ZnTPPF_{16}(SGal)_4$ was prepared in PBS from the stock solution of the PS at 10 mM.

2.4 Isolation of Exosomes from Porcine Eyecups

Exosomes used in this work were collected from porcine RPE eyecups. The porcine eyes were collected at the Beira Litoral slaughterhouse, Aveiro, Portugal. Under sterile conditions, the RPE eyecups were produced from porcine eyes by removing the anterior segment and neuronal retina. RPE eyecups were then used to produce exosomes. They were incubated with Dulbecco's Modified Eagle's Medium (DMEM)/ Ham´s F-12 Nutrient Mixture (F-12) (ATCC), supplemented with 1% exosome-depleted fetal bovine serum (FBS; Gibco), and 1% (v/v) of a mixture of penicillin, streptomycin and amphotericin B, (Sigma-Aldrich), for 30 minutes. After medium collection, an initial centrifugation at 300 x *g* for 10 minutes was performed, with a Universal 320 R centrifuge, from Hettich®. The supernatant was collected, and another centrifugation was

then carried out at 2000 x *g* (Universal 320 R) for 30 minutes, at 4 ºC. The resulting supernatant was used to isolate exosomes using the Total Exosome Isolation kit, from Invitrogen. Soon after, 0.5 mL of precipitation solution were mixed with 1 mL of supernatant and incubated overnight, at 4ºC. On the following day, the samples were centrifuged at 10000 x *g*, for 1 hour, at 4ºC, with a refrigerated microcentrifuge 1730R, from Gyrozen. The resulting pellet was resuspended in sterile PBS. Under sterile conditions, the exosomes were filtered with a 0.22 µm syringe filter (Fioroni). One aliquot of exosomes was used to quantify the concentration of protein using the BCA assay kit (described in 2.1.1.6). Exosomes were kept at -20ºC until use.

2.5 $ZnTPPF_{16}(SGal)_4$ Loading into Exosomes

For the loading of $ZnTPPF_{16}(SGal)_4$ into exosomes, two approaches were used: probe sonication and bath sonication. Per 100 µL reaction volume, different quantities of exosomes (5, 10 and 20 µL, corresponding approximately to 7.25, 14.5 and 29 µg of protein, respectively) and three concentrations of the PS (12.5, 25 and 50 µM) were tested.

The conditions of encapsulation of the PS into the exosomes were based on a previous work (Antimisiaris, Mourtas, & Marazioti, 2018). Solutions of $ZnTPPF_{16}(SGal)_4$ were freshly prepared in sterile PBS from the stock concentration at 10 mM, keeping the final concentration of DMSO of 0.5%. *Bath sonication:* After mixing the exosomes with the PS, two 30-second sonications (using an ultrasonic bath Sonorex™ TK 52 from Bandelin), separated by a 1-minute break with the sample on ice were performed. *Probe sonication:* The mixture of exosomes with PS was sonicated (with an Ultrasonic Processor for small volume applications VCX 130 from Sonics®) in two cycles of six pulses of 4s on/2s off, with a 2-minute break between cycles with the sample on ice. The probe sonicator was set at 40% amplitude.

After both procedures, the samples were incubated for 3 hours at room temperature and then purified using Centricons (Amicon Ultra-2mL with a cut-off of 10 kDa; Merck Millipore). To remove free PS (purification), three washes with PBS containing 0,5% DMSO were performed by centrifugation (with an Eppendorf® Centrifuge 5810R, made by Sigma-Aldrich®) at 7500 x *g* for 30 minutes. To recover the newly purified samples, a final centrifugation of 2 minutes at 1000 x *g* (Eppendorf® Centrifuge 5810R) with the centricons upside down was carried out. Exosomal $ZnTPPF_{16}(SGal)_4$ was placed in a 96-well black bottom plate and fluorescence was measured on a microplate reader (Synergy™ HT), with the excitation and emission filters set to 360/40 nm and 645/40 nm, respectively.

2.6 Protein Quantification

To measure the protein concentration of exosomes and total protein concentration in cell extracts, the bicinchoninic acid (BCA) assay was performed. This was carried out with a Pierce™ BCA Protein Assay Kit from Thermo Scientific.

In a transparent 96-well plate, 25 µL of sample (diluted in Milli-Q water in a proportion of 1:9) were placed into each well. For the standard curve, the concentration of the bovine serum albumin (BSA) ranged from 12.5 to 800 $\mu g.mL^{-1}$. The BCA reagent used in this assay was a mix of 50 parts of reagents A with one part of BCA reagent B, for a volume of 200 µL of BCA (A+B) reagent per well. After incubation at 37ºC for 30 min, the absorbance was measured at 570 nm on a microplate reader (Synergy™ HT). By

plotting the average absorbance at 570 nm for each BSA standard as a function of its concentration ($g.mL^{-1}$), the protein concentration in the samples was directly determined.

2.7 Nanoparticle Tracking Analysis (NTA)

For NTA, samples of exosomes and exosomes loaded with the PS were diluted in 1mL of PBS and run in a NanoSight NS300, from Malvern Panalytical. Results included mean, mode, median and concentration per particle size and were obtained with the NanoSight NTA 2.2 analytical software.

2.8 Transmission Electron Microscopy (TEM)

For TEM, exosomes and exosomes loaded with the PS were fixed in 2% paraformaldehyde (PFA) and deposited on Formvar-carbon coated grids (TAAB Laboratories Equipment). Grids were contrasted with uranyl acetate for 5 minutes. Samples were examined by electron microscopy with accelerating voltage set at 100kV. This was performed using a G2 Spirit BioTWIN electron microscope from FEI Tecnai and analyzed with its 3.2 software.

2.9 Cell Culture and Maintenance

For *in vitro* studies, a human retinal pigment epithelial cell line (ARPE-19 cell line) was obtained from the American Type Culture Collection (ATCC number: CRL-2302™). This cell line was derived from normal eyes of a 19-year-old male.
Defrosting cells: ARPE-19 cells frozen (in 10% DMSO) were quickly thawed in a 37ºC water bath and pipetted to falcons containing 5 mL of pre-warmed DMEM/F-12 culture medium. After centrifugation (Universal 320 R) at 370 x *g* for 5 minutes, the cell pellet was resuspended in fresh medium. Cells were grown in complete DMEM/F-12, with 10% (v/v) heat-inactivated FBS and 1% (v/v) antibiotic/antimycotic in 75 cm^2 cell culture flasks (Corning) and maintained at a humidified incubator at 37ºC and 5% CO_2.
Subculturing cells: When cultures reached 85-90% confluency, ARPE-19 cells were subcultured. For that, the medium was discarded, the cells were rinsed twice with warm PBS and then incubated with trypsin-EDTA (Gibco), until the cells detached from surface. After centrifugation (Universal 320 R) at 370 x *g* for 5 minutes, the cell pellet was resuspended in complete DMEM/F-12 culture medium and cells were subcultured under the above-mentioned conditions. Subcultivation was performed at ratios ranging from 1:3 to 1:5.

Moreover, to prepare cells for uptake and MTT assays, cell pellet was resuspended in medium, and viable cells were counted (from a mix of 20 μL of cell suspension with 20 μL of trypan blue) using a Neubauer chamber (or hemocytometer; VWR). The cells were seeded into 96-wellplates at a density of 3.0 x 10^4 cells/well.

2.10 Incubation of ARPE-19 Cells with $ZnTPPF_{16}(SGal)_4$ and Exosomal $ZnTPPF_{16}(SGal)_4$

ARPE-19 cells were seeded on 96-well plates at 30000 cells per well and cultured for 24 hours at 37 ºC and with 5% CO2 and 95% air. On the next day, the medium was removed, cells washed with PBS and incubated with freshly prepared $ZnTPPF_{16}(SGal)_4$ (0.5-15 μM) or exosomal $ZnTPPF_{16}(SGal)_4$ (0.5-3 μM) in 50 μL of PBS or DMEM/F-12 containing 1% FBS, in dark conditions. For the incubation with the $ZnTPPF_{16}(SGal)_4$ exosomal, we have chosen the condition in which mixtures of 10 μl exosomes with 50 μM $ZnTPPF_{16}(SGal)_4$ for a total volume 100 μL, were performed. The cells were exposed to $ZnTPPF_{16}(SGal)_4$ or exosomal $ZnTPPF_{16}(SGal)_4$ for selected time points (1 to 24 hours) in the humidified incubator gassed with 5% CO_2 and 95% air. In all experiments, the concentration of DMSO was kept less than 0.5% (v/v). Triplicates of each condition were considered in the assay.

2.11 Determination of Intracellular Concentration of $ZnTPPF_{16}(SGal)_4$

Since the porphyrin $ZnTPPF_{16}(SGal)_4$ exhibits fluorescent properties, its intracellular accumulation was assessed by fluorimetry. After incubation with free $ZnTPPF_{16}(SGal)_4$ or exosomal $ZnTPPF_{16}(SGal)_4$, cells were washed twice with 100 μL of sterile PBS and then lysed in 120 μL of 1% (m/v) SDS in PBS, pH of 7.0. After a quick homogenization on the shaker, 90 μL were removed from each well and plated in a black 96-multiwell plate. The shaker used in this work was a PSU-20i, a multi-functional orbital shaker from Biosan. Fluorescence was assessed with a microplate reader (Synergy™ HT), using the excitation and emission filters set to 360/40 nm and 645/40 nm, respectively. With the aim of normalizing fluorescence data to total protein quantity, a BCA assay was performed for each sample.

2.12 Photodynamic Assays

After incubation with the PS, detailed in 2.1.2.2, free and carried by exosomes, 100 μL of PBS were used to wash out the samples from all wells. PBS was removed soon after and 200 μL of fresh DMEM/F-12 with 10% FBS were added to each well. Using the LED system, (described in 2.1.1.3), one of the plates was irradiated for 40 minutes, whilst the other was kept in the dark, but otherwise in the same conditions, ensuring PDT was the only factor differentiating the two. Following PDT, plates were placed inside the humified incubator, at 37ºC, where they stayed for about 24 hours.

2.13 ARPE-19 Cell Viability Assays

For MTT colorimetric assays, ARPE-19 cells were seeded at a density of 30,000 cells per well in 96-well plates. The following day, the cells were incubated with the PS and photodynamic treatment was performed, as described in 2.1.2.2. and 2.1.2.4, respectively. Twenty-four hours after treatment, 150 μL of DMEM:/F12 medium were removed from every well of both plates. Soon after, 10 μL of 3-[4,5-dimethylthiazol-2-

yl]-2,5-diphenyltetrazolium bromide (MTT; Sigma-Aldrich), at a concentration of 3 $mg.mL^{-1}$ were added to each of them, in dark conditions. The cells were then incubated in the humidified incubator for 4 hours, enabling the formation of formazan crystals. The resulting purple needle-shaped crystals were dissolved by the addition of 150 μL of a solution of 0.04 M of acidic isopropanol. Since these crystals do not dissolve by the simple addition of this solution, up and down pipetting was performed in every well until all crystals disappeared. The absorbance was measured at 570 nm (using 620 nm as the background wavelength) using the microplate reader (Synergy^{TM} HT). The percentage of viable cells was obtained using the following equation:

$$\textit{MTT reduction (\%)} = \frac{(Absorbance\ at\ 570\ nm - Absorbance\ at\ 620\ nm)_{PS\ treated\ samples}}{(Absorbance\ at\ 570\ nm - Absorbance\ at\ 620\ nm)_{Control\ samples}} \times 100\%$$

2.14 Laser-induced model of CNV

All animal procedures were performed according to the decree law nº 113/2013 (a national legislation that transposes the European directive 63/2010/CE) and other related legislations. Moreover, this study was approved by the Animal Welfare Committee of the Coimbra Institute for Clinical and Biomedical Research (iCBR), Faculty of Medicine, University of Coimbra and the Portuguese Veterinary Direction (ORBEA: 03/2021). All the procedures carried out on animals were performed by a researcher (MSc Joana Martins) with an accreditation for animal research from the same entity (Ministerial directive 1005/92).

Wild-type C57BL/6J mice (pigmented mice) were born and raised at the bioterium of Coimbra's Institute for Clinical and Biomedical Research. Throughout the animal model, mice were kept in individually ventilated cage systems and fed with a standard laboratory diet, including water intake.

The CNV induction model, based on the works of S. J. Ryan (Ryan, 1979), Gong (Gong, et al., 2015) and Balser (Balser, Wolf, Herb, & Langmann, 2019), started with the preparation of the anesthesia. Starting from stock solutions of Nimatek (ketamine) and Sedator (medetomidine), both from Dechra, at concentrations of 100 $mg.mL^{-1}$ and 1 $mg.mL^{-1}$, respectively, mixtures of the two were prepared for each animal in a saline solution of 0,9% NaCl, with the aim of delivering 75 $mg.kg^{-1}$ of Nimatek and 1 $mg.kg^{-1}$ of Sedator per animal. After anesthesia preparation, the subject was intraperitoneally injected with it, quickly fell asleep, and drops of 10 $mg.mL^{-1}$ of Tropicil Top® (tropicamide), a pupil dilator, and 4 $mg.mL^{-1}$ of Anestocil® (oxybuprocaine), a topical anesthetic, both from Edol, were topically administered to eyes of the mice. Celluvisc® (carmellose sodium) 1% w/v, an Allergan product, was also topically applied to the eyes throughout the whole procedure. Laser irradiation was performed in both eyes, with a Vitra^{TM} 2 laser, by Quantel Medical, focusing on four different spots, with specific laser settings (Power: 120 mW; Spot size: 50 μm; Pulse duration: 100 ms), with the assistance of a slit lamp and a coverslip (in contact with the eye). These laser spots were distributed in square or diamond shapes, across four different quadrants, since they were meant to be equally distanced between themselves and to the optic nerve, around double the diameter of the optic nerve disc.

2.14.1 Optical Coherence Tomography (OCT)

Eye fundus photographs and cross-sectional images of the retina were taken by spectrum-domain OCT using a Phoenix Micron™ IV Retinal Imaging Microscope (Phoenix Technology Group) before and immediately after laser irradiation, as well as at days 3, 7, and 14 after laser photocoagulation.

2.14.2 Fluorescein Angiography

Fluorescein angiography was performed using the Phoenix Micron™ IV at days 7 and 14 after laser photocoagulation. For this procedure, mice were anesthetized, in the same conditions described for CNV induction. After falling asleep, they were intraperitoneally injected with 5% fluorescein sodium, to better visualize the retinal and choroidal vessels and the laser-induced lesions. In some cases, Revazol (atipamezole hydrochloride), from Dechra, with an initial concentration of $5mg.mL^{-1}$, was also administered at a concentration of 10 $mg.kg^{-1}$, thus reversing the sedating effects of medetomidine, awakening the mice within minutes. Mice were sacrificed on day 15 by transcardial perfusion.

2.14.3 Tissue Preparation and Immunohistochemistry

Mice were anesthetized, in the same conditions described for CNV induction. Soon after falling asleep, its abdominal cavity was cut open, the sternum was opened, and a catheter was placed inside the left ventricle. Thereafter, a transcardial perfusion with warmed PBS was made, cleansing all blood traces, followed by another one with warmed 4% PFA in 0.1 M PBS, fixating all tissues. Eyes were enucleated and postfixed with 4% PFA. The cornea was then carefully removed. After one hour in PFA, eyes were washed with PBS and cryoprotected with 15% and 30% sucrose. The eyecups were covered with a mixture of embedding medium (Shandon Cryomatrix™, Thermo Scientific) with 30% sucrose in a proportion of 1:1, and frozen at -80°C. Retinas were sectioned into 14 µm sections using a freezing microtome (Leica CM3050 S cryostat, from Leica Biosystems). Retinal cross-sections were collected onto Menzel-Gläser Superfrost® Plus glass slides, from Thermo Scientific, and stored at -20°C until immunostaining.

For immunohistochemistry on mouse retinal sections, the cryosections were air dried for 30 minutes. Sections were then fixed in cold acetone (-20°C) for 10 min, washed several times with PBS, permeabilized with a 1% Triton X-100 solution (Sigma-Aldrich®) in PBS for 15 minutes. After washing with PBS and blocking with 0.02% BSA Fraction (Sigma-Aldrich) and 0.25% Triton X-100 in PBS for 30 minutes, slices were incubated in primary antibodies (rabbit polyclonal Ki67 (Abcam, # Ab15580) and mouse monoclonal alpha-smooth muscle actin (αSma; Santa Cruz Biotechnology, #sc-53142), 1:100 dilutions in 0.02% BSA and 0.25% Triton X-100 in PBS), for 90 minutes, in a humidity chamber (built inside a StainTray™ Slide Staining System). One section was incubated with 5% BSA in PBS, as a negative control. Sections were rinsed with PBS and incubated with secondary antibodies (Alexa fluor 550 anti-mouse (1:200) and Alexa fluor 488 anti-rabbit (1:200)) diluted in PBS containing DAPI (1:5000) for 1 hour, protected from light. After washing several times with PBS, sections were mounted with glycergel (Glycergel Mounting Medium, from Dako) and covered with coverslips. Samples were imaged using a confocal microscope (LSM 710 confocal microscope, Carl Zeiss).

2.15 Statistical Analysis

The results are presented as mean ± standard error. One-way ANOVA followed by Tukey´s or Kruskal-Wallis' tests, employed to calculate the statistical difference between three or more groups. Data analyses and graphical presentations were performed using GraphPad Prism 8.0.1. P-value was considered at the 5% level of significance to deduce inference of the significance of the data.

Chapter III

Results and Discussion

3.1 Photophysical Characterization

$ZnTPPF_{16}(SGal)_4$ (a zinc porphyrin conjugated with four molecules of galactose) shows a characteristic absorption spectrum of porphyrins, with an intense band between 400-420 nm (Soret band) and a weaker band between 540-580 nm (Q band). Fig. 3.1 displays the absorption spectra of $ZnTPPF_{16}(SGal)_4$ in DMSO (A) and in an aqueous solution (B). The optical density of both Soret (maximum at 415 nm) and Q bands are higher in DMSO than in an aqueous solution.

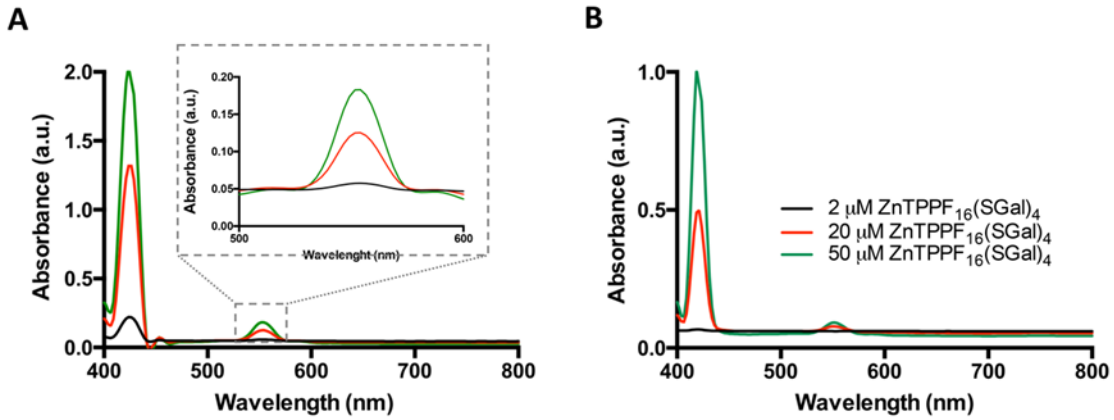

Figure 3.1. Absorption spectra of 2 (black line), 20 (green line) and 50 μM (red line) $ZnTPPF_{16}(SGal)_4$ in (A) DMSO and (B) PBS containing 0.5% DMSO and 1% SDS.

The broadening of the bands is related with a reasonable solubility of $ZnTPPF_{16}(SGal)_4$ in aqueous solution. However, its behavior in DMSO and aqueous solution did not follow strictly the Beer-Lambert at the studied concentrations tested, which suggest that some aggregation may exist.

The photostability of $ZnTPPF_{16}(SGal)_4$ was investigated to assess its potential for PDT. When in PBS solution, $ZnTPPF_{16}(SGal)_4$ showed to be very stable in the dark conditions. Light irradiation for 40 min did not also induce a significant absorption decrease (at 415 nm) of $ZnTPPF_{16}(SGal)_4$ in PBS solution (Fig. 3.2). It was important to guarantee that the PS did not experience considerable degradation when exposed to visible light. The good photostability of $ZnTPPF_{16}(SGal)_4$ upon 40 min of light irradiation allowed us to establish that it would be promising for *in vitro* PDT assays.

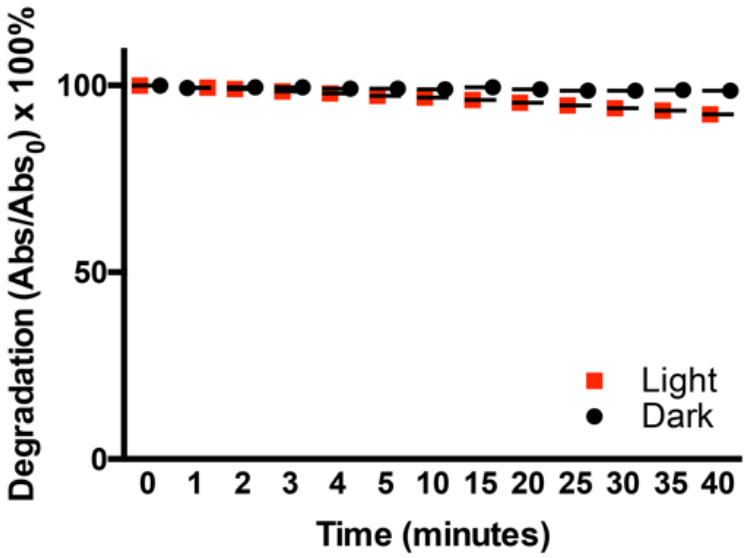

Figure 3.2. Stability of 20 µM ZnTPPF$_{16}$(SGal)4 in PBS (with 0.5% DMSO) in dark conditions (black) and under white LED at a fluence rate of 8.4 mW.cm^{-2}.

Other properties of ZnTPPF$_{16}$(SGal)$_4$ such as its potential to generate $^1O_2$ are relevant for photoinduced processes in PDT, although they were not investigated in this study.

3.2 Manufacture and Characterization of Exosomal ZnTPPF$_{16}$(SGal)$_4$

The main goal was to devise a new approach for bettering AMD management by focusing on fibrosis and CNV. Exosomal ZnTPPF$_{16}$(SGal)$_4$ was originated to test the ability of exosomes to deliver ZnTPPF$_{16}$(SGal)$_4$ to fibroblast-like cells. Given the potential of EVs to serve to cell-to-cell communication, this approach could provide a significant benefit in terms of more efficient PS delivery to fibroblast-like and endothelial cells of choroidal neovessels in patients with wet AMD.

As a source of exosomes, we used porcine eyecups with the RPE exposed to the culture medium. Although ultracentrifugation is the gold standard for exosome isolation (Antimisiaris, Mourtas, & Marazioti, 2018), we have chosen a commercially available isolation reagent kit. The main benefit of using this kit was that it produced a high yield of exosomes while also being a simple and rapid procedure that did not require any extra equipment. TEM was used to analyze exosomes isolated from conditioned media bathing the RPE surface of pig eyecups in terms of morphology and size (Fig. 3.3). They showed a round-shaped vesicular morphology, and their size varied from 50 to 80 nm (Fig. 3.3A), which is consistent with what has been reported in the literature (Antimisiaris, Mourtas, & Marazioti, 2018). When we characterized the RPE-derived exosomes using NTA, we found that mean particle diameter and modal diameter are about 145 nm and 115 nm, respectively (Fig. 3.3B). Although the origin of released exosomes was not confirmed, the content of a RPE marker, such as RPE65, could indicate whether exosomes are mostly produced from RPE cells (Klingeborn, et al., 2017).

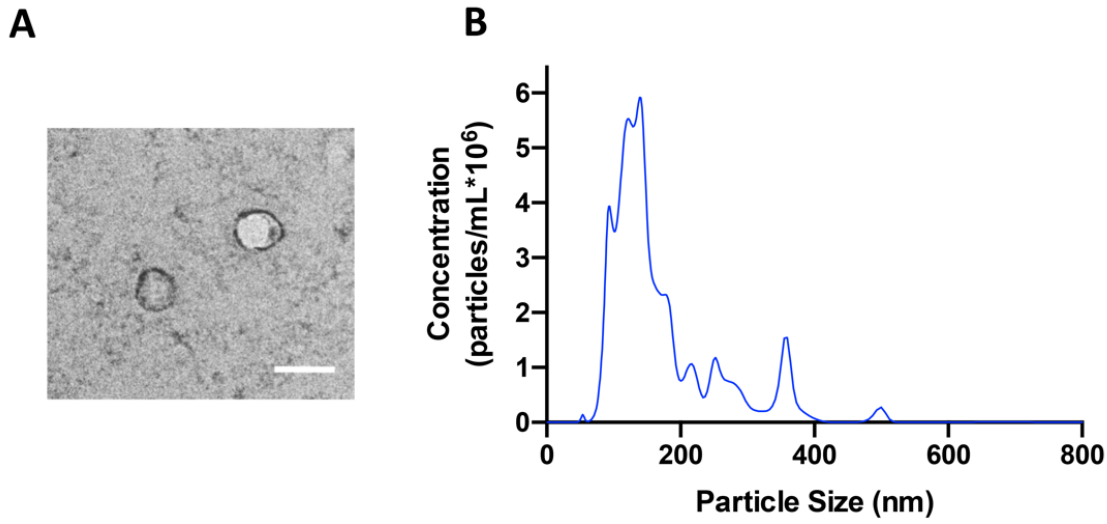

Figure 3.3. **Exosomes isolated from conditioned medium bathing the RPE surface (30 min of incubation) of porcine eyecups.** Exosomes released by porcine eyecups under control conditions (in DMEM/F-12, GlutaMAX containing 1% exo-free FBS) were isolated using Total Exosome Isolation kit, filtered, and analyzed by (A) TEM and (B) NTA. (A) Representative image of EVs released by pig eyecups visualized by TEM. Scale bar 100 nm (B) NTA showing the concentration of EVs from porcine eyecups when a solution of 100 μL was prepared with 10 μL of the exosome sample.

One of the most significant drawbacks of EVs as a potential drug delivery system is their inability to properly load drugs. Exosome loading has been examined using a variety of methods, including a simple incubation of the vesicles with lipophilic molecules and hydrophobically modified compounds, repetitive freezing-thawing techniques, saponin permeabilization, extrusion, sonication, and electroporation (Villa, Quarto, & Tasso, 2019).

Bath sonication and probe sonication, both in combination with passive diffusion, were used in this work. Different quantities of exosomes from eyecups and PS in concentrations ranging from 12.5 to 50 μM were tested (Fig. 3.4A). Entrapped $ZnTPPF_{16}(SGal)_4$ into exosomes were purified using Centricons® (Centrifugal purification device), with a cut-off of 10 kDa. If we assume that free PS has around 1.8 kDa, it is expected that it passes through the filter. Based on the fluorescent characteristics of the PS, fluorescence spectroscopy (Synergy^{TM}) was used to assess the loading efficiency of the PS into the exosomes. For that, fluorescence after bath sonication or probe sonication and after purification of exosomal $ZnTPPF_{16}(SGal)_4$ for each of the conditions used, was measured (Fig. 3.4).

A

Conditions (V_t=100 µL)	[$ZnTPPF_{16}(SGal)_4$] µM	Vol. Exo µL	Quantity of protein in Exo µg
A	-	10	14.5
B	12.5	10	14.5
C	25	10	14.5
D	50	5	7.25
E	50	10	14.5
F	50	20	29.0

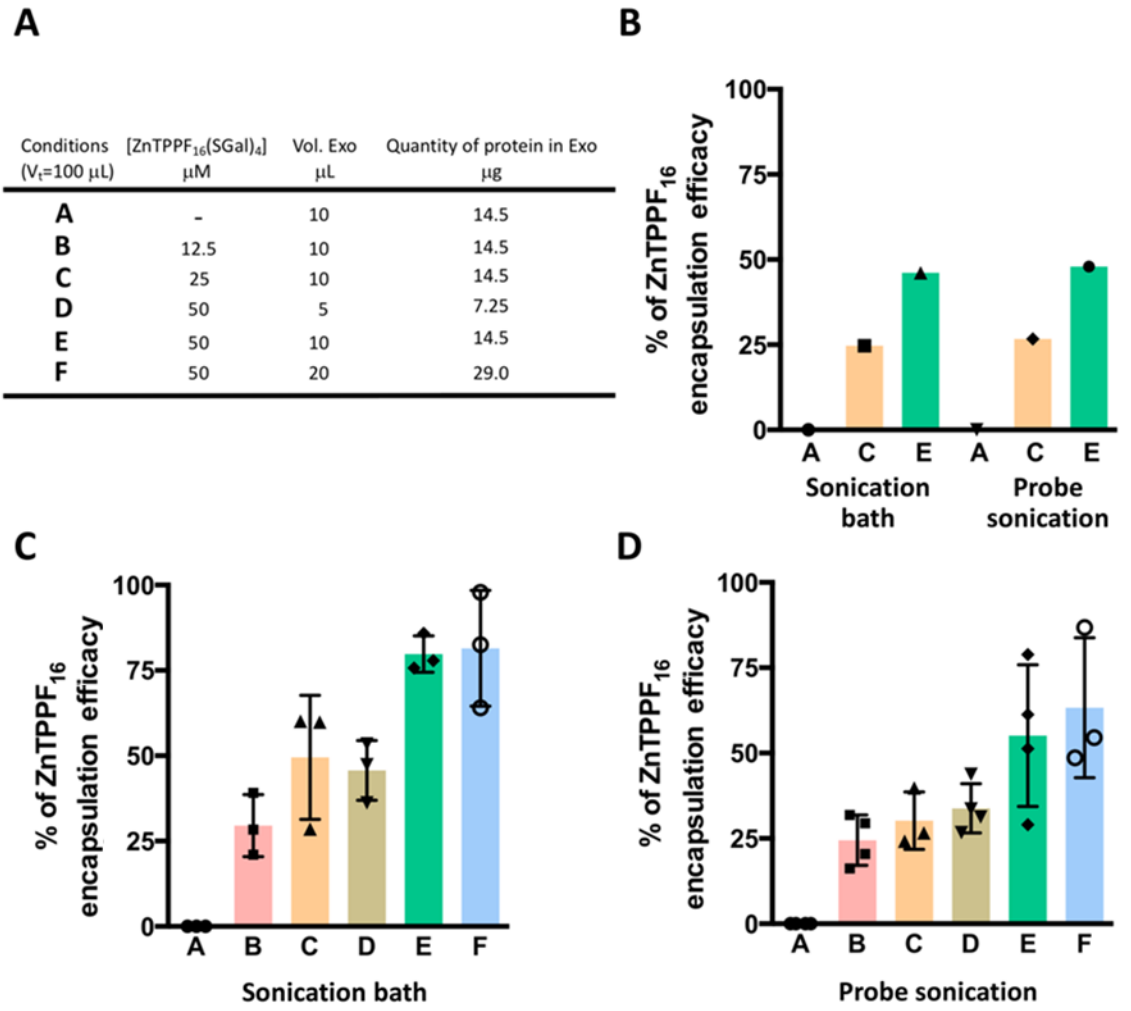

Figure 3.4. **$ZnTPPF_{16}(SGal)_4$ encapsulation efficacy.** (A) Conditions tested with different amounts of exosomes (5, 10 and 20 µL) and PS (0, 12.5, 25 and 50 µM) used in PS encapsulation studies. (B) PS encapsulation efficacy after exosomal permeabilization using sonication bath and probe sonication; (C) PS encapsulation efficacy with a 3-hour period of passive diffusion after exosomal permeabilization using sonication bath. (D) PS encapsulation efficacy with a 3-hour period of passive diffusion after exosomal permeabilization using probe sonication.

Passive diffusion for 3 hours after sonication bath or probe sonication (Fig. 3.4C&D) led to a higher loading efficacy compared to the condition in that exosomal purification was performed shortly after sonication (Fig. 3.4B). For the conditions using 10 µL of exosomes in the mixture, the encapsulation efficacy increased in a concentration-dependent manner. The sonication bath improved the encapsulation efficiency compared to probe sonication. For instance, considering the condition in which 10 µL of exosomes and 50 µM PS were used, a higher loading efficiency was obtained, about 80% and 55% for sonication in an ultrasonic bath and probe sonication, respectively (Fig. 3.4C & D). However, doubling the number of exosomes (to 20 µL) did not lead to a significant increase in the loading efficacy of any of the conditions tested.

According to Antimisiaris et al. (Antimisiaris, Mourtas, & Marazioti, 2018), passive diffusion, which is achieved by incubation of a drug with EVs, usually results in

a poor loading efficacy, depending on the lipophilic properties of the drug and the concentration gradient. Due to this drawback, both sonication bath and probe sonication approaches were used, which are known to cause deformations in exosome membranes, most likely by the development of temporary holes (Haney, et al., 2015). Under sonication, reformation of exosomal membranes may allow drugs to penetrate through lipid bilayers (Soo Kim, et al., 2016). In this study, the combination of diffusion with the sonication procedure enhanced PS incorporation/association efficiency. However, the stability of both the $ZnTPPF_{16}(SGal)_4$ structure and exosomal $ZnTPPF_{16}(SGal)_4$ were not explored in this work.

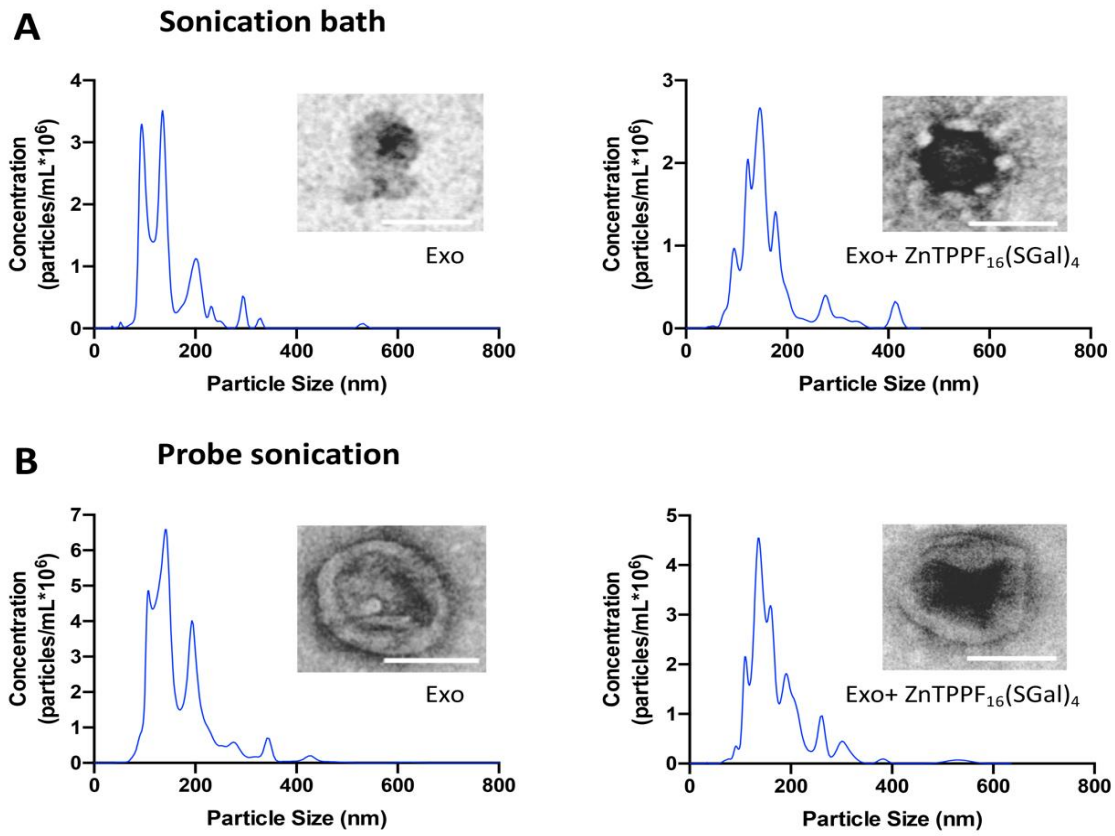

C

	Sonication bath		Probe sonication	
	A	E	A	E
Concentration (particles/mL)	$1.25x10^8 \pm 8.68x10^6$	$1.03x10^8 \pm 5.46x10^6$	$2.64x10^8 \pm 1.88x10^7$	$1.57x10^8 \pm 7.11x10^6$
Mean (nm)	130±3.0	146±7.3	151±3.9	157±2.5
Mode (nm)	109±8.2	153±6.7	131±5.3	146±5.9

Figure 3.5. Particle concentration, size distribution profile and TEM of exosome samples and exosomal $ZnTPPF_{16}(SGal)_4$ from pig eyecups. (A) Exosomal $ZnTPPF_{16}(SGal)_4$ preparation after exosomes permeabilization with sonication bath and (B) probe sonication. (A) and (B) TEM images of exosomal $ZnTPPF_{16}(SGal)_4$. Triplicates to quintuplicates measurements of the same sample were measured. Scale bar: 100 nm.

Exosomal $ZnTPPF_{16}(SGal)_4$ formulations were analysed by NTA (Fig 3.5A&B). The concentration of exosomes in solution without PS and any sonication was $2.99x10^8 \pm 1.37x10^7$ particles/mL. Although sonication bath and probe sonication followed by centrifugation in Centricons® showed a decrease in the concentration of the particles, their morphology was not impaired as observed by TEM (Fig. 3.5A&B). When $ZnTPPF_{16}(SGal)_4$ loading was conducted, the modal diameter of the vesicles increased (Fig. 3.5A,B&C). Interestingly, exosomal $ZnTPPF_{16}(SGal)_4$ formulations presented denser vesicles comparing with vesicles that were not loaded with the drug, which suggests encapsulation/association of the zinc (II) metalated porphyrin (Fig. 3.5A&B). The membrane appeared to be intact as well. Although these findings suggest that the PS is encapsulated, further studies are needed to determine whether the PS is loaded in the exosomes or is associated with their surface. Scanning Electron Microscopy, a 3D imaging technology based on the same principle as TEM, the employment of electron beams to detect nanoparticles, is one viable option. (Wu, Deng, & Klinke II, 2015).

Following the outcome of NTA, we assumed a loss of exosomes was occurring either during permeabilization (sonication) and/or purification (in Centricons®), decreasing the concentration of these vesicles. However, this hypothesis should be further investigated by Diffuse Light Scattering, the most common technique used in the assessment of the size distribution of nanoparticles (Kim, Beng Ng, Bernt, & Cho, 2019).

Table 3.1. Protein concentration of exosomes or exosomal $ZnTPPF_{16}(SGal)_4$.

		Sonication bath		Probe sonication	
	Exosomes	A	E	A	E
[Protein], μg/μL	1.47±0.02	1.35±0.08	1.35±0.08	1.34±0.12	1.35±0.16

Data are presented as mean ± SD.

We noticed a small decrease in protein concentration after exosomal permeabilization, consistent with the lower vesicles´ concentration after the two sonication methods and purification in Centricons® (Table 3.1). We also measured the protein concentration of exosomes after their permeabilization, but before the purification in Centricons®. We found that exosomal permeabilization may have slightly affected protein concentration (Concentration of exosomal protein after permeabilization: i) Sonication bath: A – 1.39 ± 0.092 mg/mL; E – 1.37 ± 0.093 mg/mL; ii) Probe sonication: A – 1.35 ± 0.11 mg/mL; E - 1.38 ± 0.14 mg/mL). These results are consistent with the exosome loss seen by NTA (Fig. 3.5) and revealed it was mostly due to sonication. This loss in protein concentration was expected since studies report that sonication can compromise the integrity of the exosome's membrane (Luan, et al., 2017). To reestablish its integrity, Luan et al. suggested an incubation at 37°C, which could be a possible solution to overcome exosome loss.

3.3 Cellular Uptake of Free $ZnTPPF_{16}(SGal)_4$ by ARPE-19 Cells

In vitro research began with the assessment of cellular uptake of free $ZnTPPF_{16}(SGal)_4$. In previous PDT studies from our group, the incubation of the cells with PSs was usually in PBS and for a short period. Since we were interested in performing cellular uptake assays with the exosomal $ZnTPPF_{16}(SGal)_4$ for long periods, we began by comparing free $ZnTPPF_{16}(SGal)_4$ uptake in PBS against DMEM/F-12 supplemented with 1% FBS.

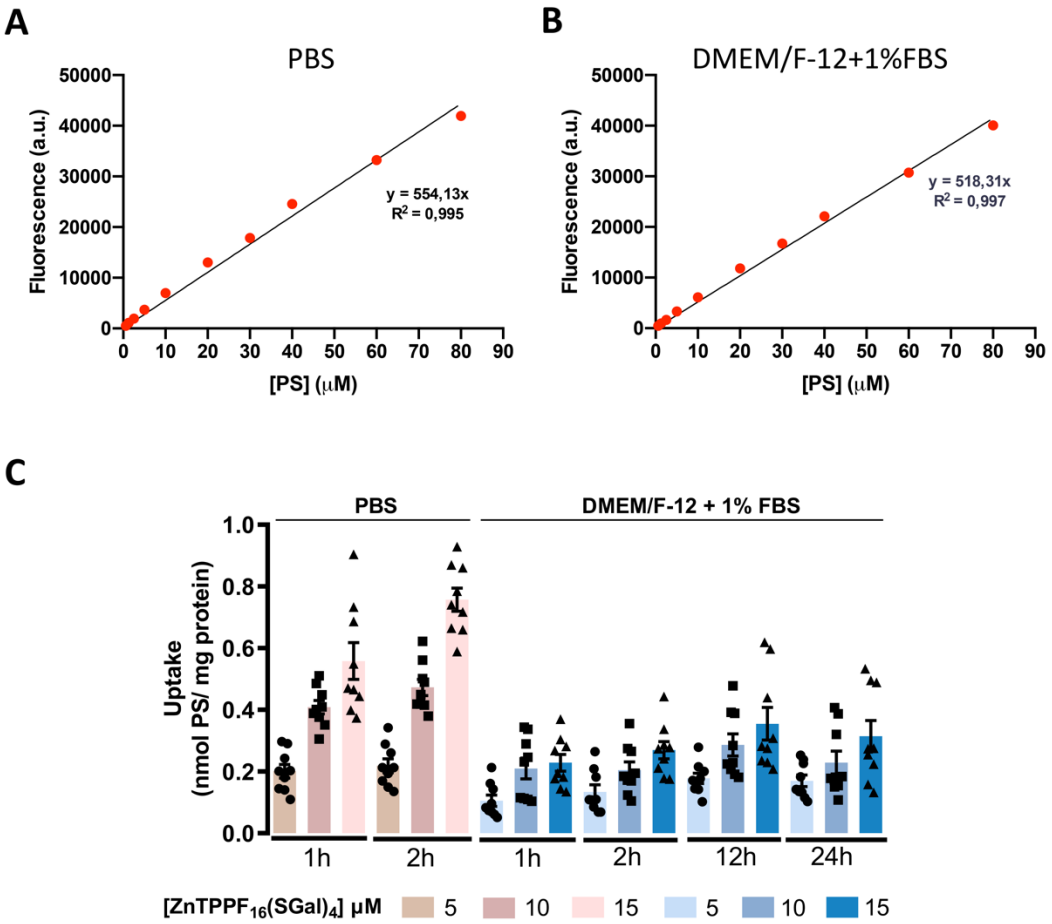

Figure 3.6. Cellular uptake of free $ZnTPPF_{16}(SGal)_4$ by ARPE-19 cells. (A) Calibration curves of the fluorescence of $ZnTPPF_{16}(SGal)_4$ in (A) PBS and (B) DMEM/F-12 + 1% FBS and. (C) ARPE-19 cells were incubated with increasing concentrations of $ZnTPPF_{16}(SGal)_4$ (5, 10 and 15 μM) for different period times in PBS or DMEM/F-12 supplemented with 1% FBS. PS intracellular accumulation was assessed by fluorimetry and normalized to protein concentration. Data are the mean value ± SEM of three independent experiments performed in triplicates.

The first step was to create calibration curves with known PS concentrations for both solutions. With this purpose in mind, several concentrations of PS prepared in DMEM/F-12 supplemented with 1% FBS and PBS (all containing 0.5% DMSO) were evaluated by fluorescence spectroscopy, yielding the calibration curves shown in Fig. 3.6A&B. There was a similar linear relationship between fluorescence intensity and concentration of the PS in the two tested incubation solutions. For assessment of the

cellular uptake of the PS, ARPE-19 cells were incubated with increasing concentrations of free PS (5, 10, and 15 μM, all with 0.5% DMSO) in PBS, for 1 hour and 2 hours and DMEM/F-12 supplemented with 1% FBS, for up to 24 hours. Although the cellular uptake of $ZnTPPF_{16}(SGal)_4$ was concentration- and time-dependent for both incubation solutions, except for the 24-hour incubation in DMEM/F-12, the intracellular accumulation of the PS up to 2 hours of incubation was significantly increased in PBS against medium containing FBS (Fig. 3.6C).

Even though the calibration curves in PBS and DMEM/F-12 are similar, the fact that fluorescence was read immediately after the preparation of the working solutions may have influenced these findings. To verify whether longer periods lead to aggregation or changes in fluorescence properties of the PS, calibration curves with the same incubation periods used for cellular uptake (1h, 2h, 12h, and 24h), should have been performed. Concerning the differences obtained for cellular uptake between PBS or DMEM supplemented with 1%FBS, we postulated that a possible interaction between the FBS and the PS, which could impair the PS´ fluorescent properties or prevent it from being recognized by the cells, could be the reason for the low values of cellular uptake, which is based on the fluorescence of the compound.

3.4 Toxicity of Free $ZnTPPF_{16}(SGal)_4$ in ARPE-19 cells in dark conditions and after light irradiation

One of the properties a PS should possess to be suitable for PDT is the absence of cytotoxicity *per se* in the absence of light (dark). The toxicity in dark conditions of $ZnTPPF_{16}(SGal)_4$ in ARPE-19 cells was examined 24 hours after treatment by the MTT colorimetric assay. Cells were incubated with 5, 10 and 15 μM of PS for 1, 2, 12 and 24 hours in darkness. As expected, non-irradiated cells did not present significant changes in cellular viability after PS incubation (Fig. 3.7A). When cells were incubated with the PS and then irradiated using a LED system, for 40 min, there was a significant decrease in cell viability (Fig. 3.7B). Moreover, phototoxicity was greater when incubation for 1 hour with the PS (only up to 10 μM) was performed in PBS comparatively to DMEM/F-12. The increase in phototoxicity was concentration- and time-dependent (Fig. 3.7B). The lower phototoxicity found in DMEM/F-12 solutions can be related to the lower cellular uptake, as mentioned previously. For example, one study reported a significant influence of FBS in the cytotoxicity of biodegradable metals (Jablonská, Kubásek, Vojtech, Ruml, & Lipov, 2021).

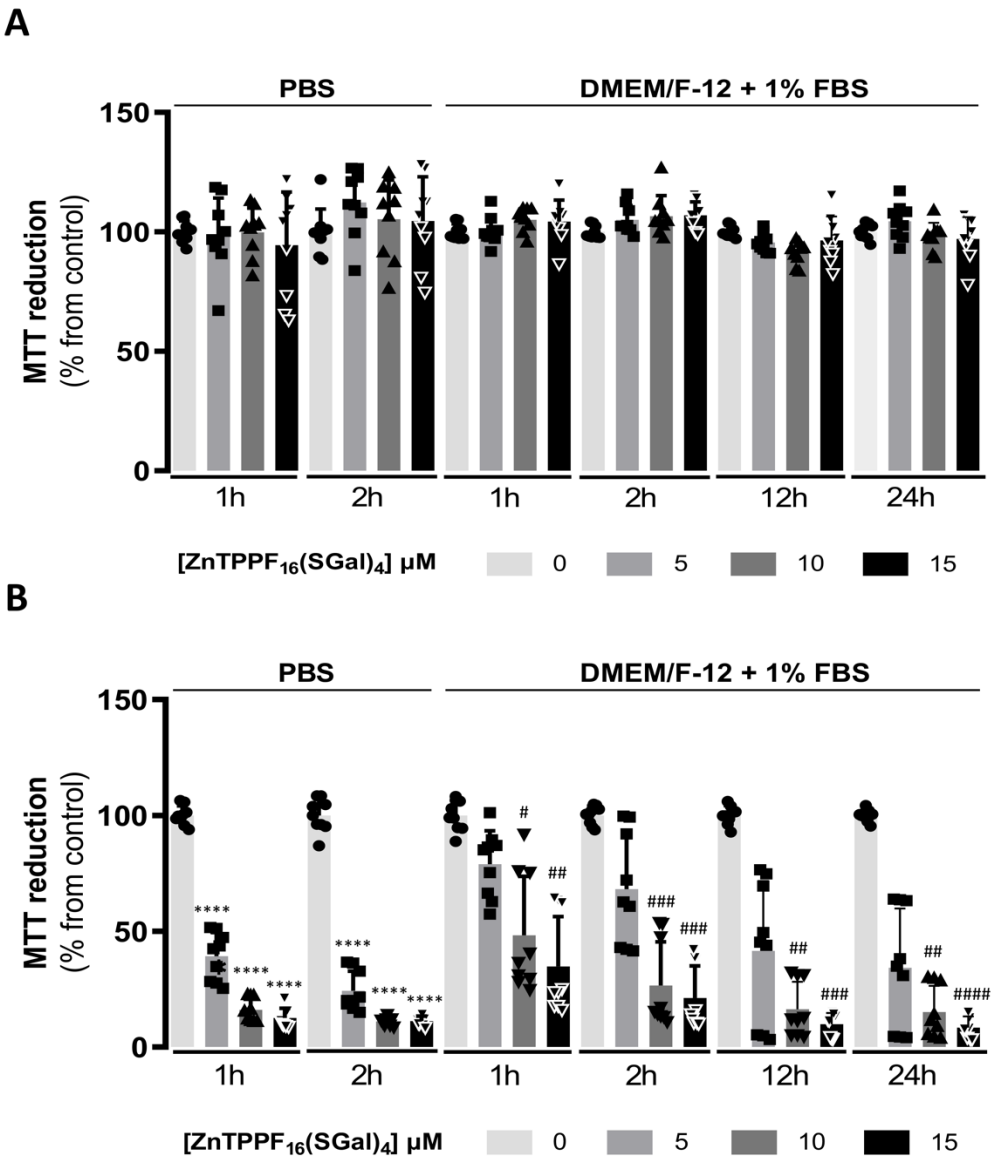

Figure 3.7. ZnTPPF$_{16}$(SGal)$_4$ toxicity in ARPE-19 cells in the dark (A) and after light irradiation (B). ARPE-19 cells were incubated with ZnTPPF$_{16}$(SGal)$_4$ at various concentrations (5, 10, and 15 µM) for up to 2 hours in PBS and 24 h in DMEM/F-12, in dark conditions. Cell viability was assessed 24 hours after treatment (dark or after irradiation with LEDs at 8.4 mW.cm^{-2} for 40 min) using the MTT colorimetric assay. The percentage of cytotoxicity was calculated relatively to control cells (cells incubated with PBS or DMEM/F-12). Data are the mean value ± S.E.M. of three independent experiments performed in triplicates. ****P<0,0001) significantly different from control cells at the same time point (in PBS). One-way ANOVA followed by Tukey´s multiple comparison test. $^{\#}P$<0.05, $^{\#\#}P$<0.01, $^{\#\#\#\#}P$<0.001 and $^{\#\#\#\#\#}P$<0.0001 significantly different from control cells at the same time point (in DMEM/F-12). One-way ANOVA followed by Dunn´s multiple comparison test.

3.5 Cellular Uptake of Free vs Exosomal ZnTPPF$_{16}$(SGal)$_4$ by ARPE-19 Cells

After drug loading trials, the delivery capability of exosomal ZnTPPF$_{16}$(SGal)$_4$ was investigated. After we found that the free PS is quite effective for concentrations higher than 10 μM, we assessed whether the compound carried in exosomes is an asset over the free compound, by testing low concentrations of the compound.

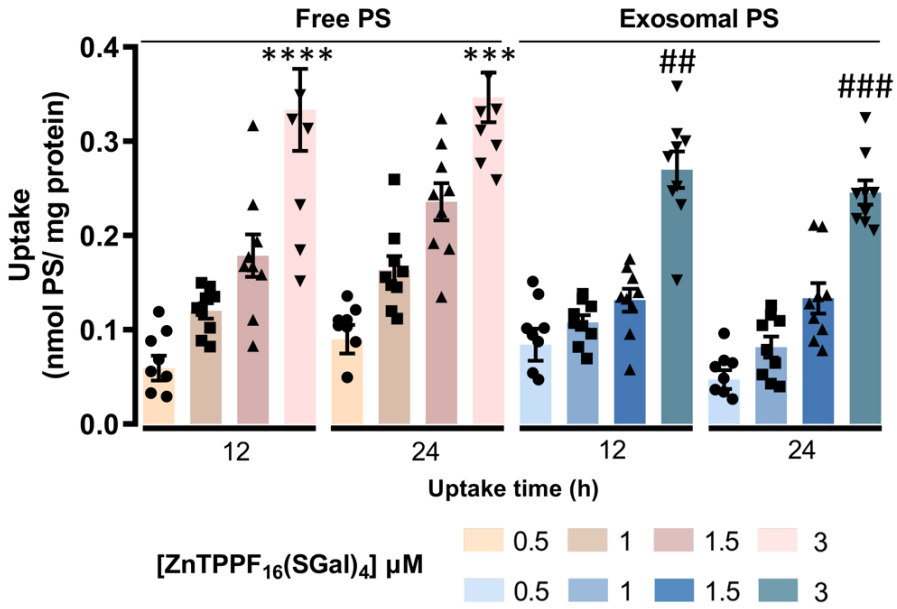

Figure 3.8. Intracellular accumulation of free and exosomal ZnTPPF$_{16}$(SGal)$_4$ in ARPE-19 cells. ARPE-19 cells were incubated in the dark with various concentrations (0.5, 1, 1.5 and 3 μM) in DMEM/F-12 supplemented with 1% FBS at concentrations, for 12 and 24 hours. The intracellular accumulation of the PS was determined by fluorometry and normalized to total protein quantity. Results are the mean value ± SEM of at least three independent experiments performed in triplicates. ***P<0.001, ****P<0.0001 significantly different from cells incubated with 0.5 μM of free PS, at the same time point. $^{\#\#}P$<0.01, $^{\#\#\#\#}P$<0.001 significantly different from cells incubated with 0.5 μM of exosomal PS, at the same time point. No significant changes found between the free form of the PS and exosomal PS for the concentration and time point. One-way ANOVA followed by Kruskal-Wallis multiple comparison test was performed.

Exosomal ZnTPPF$_{16}$(SGal)$_4$ generated the previous day was incubated in ARPE-19 cells at the same nanomoles utilized in free PS administration. For both the 12- and 24-hour incubation periods, although there was a tendency to an increase in the cellular absorption of ZnTPPF$_{16}$(SGal)$_4$ for free PS compared to exosomal PS, the differences were not statistically significant (Fig. 3.8). Moreover, cellular uptake was concentration-dependent. According to these results, the use of exosomes as drug carriers did not lead to enhanced PS internalization in fibroblast-like cells, the ARPE-19. Exosomes came from a different species (swine) and cell type (RPE cells) than the target cells (human origin and fibroblast-like). The vesicles usually carry important features of the parental cells and can act on the cell itself (have an autocrine activity) (Antimisiaris, Mourtas, & Marazioti, 2018). We used the native RPE as a source of exosomes for PS loading

purposes as a proof-of-concept in our investigation, even though it was not the best choice. Following this study, the assessment of PDT effect of exosomal $ZnTPPF_{16}(SGal)_4$, with exosomes derived from ARPE-19 cells would be of interest.

3.6 Toxicity of Free vs Exosomal $ZnTPPF_{16}(SGal)_4$ in ARPE-19 cells in Dark Conditions and after Light Irradiation

The following step of this study was to understand how exosomal PS affects cellular viability in the dark and after light irradiation, in comparison with free PS. The toxicity in dark conditions of $ZnTPPF_{16}(SGal)_4$ and exosomal $ZnTPPF_{16}(SGal)_4$ on ARPE-19 cells was examined 24 hours after treatment by MTT. As we intended to assess whether the exosomal PS would be of added value over the PS in its free form, lower concentrations were tested. The cells were incubated for 12 hours or 24 hours in darkness with 0.5, 1, 1.5 and 3 μM PS. As expected, $ZnTPPF_{16}(SGal)_4$ and exosomal $ZnTPPF_{16}(SGal)_4$ were not toxic in the absence of light (Fig. 3.9A). Exosomal PS incubation for 12 and 24 hours revealed no cytotoxicity, indicating that using exosomes as a PS carrier is safe.

For the PDT assays, ARPE-19 cells were incubated with free and exosomal $ZnTPPF_{16}(SGal)_4$ at various concentrations (0.5, 1, 1.5 and 3 μM) for 12 or 24 hours in the dark and then irradiated for 40 min. Similar to what was observed for higher concentrations, the PS in its free and exosomal forms at lower concentrations induced phototoxicity in a concentration- and time-dependent manner. However, for all the concentrations tested, the differences in MTT reduction were not statistically significant between free PS and exosomal PS (Fig. 3.9B). Here, we did not see the expected increase in cell death for exosomal PS samples, contrarily to a previous study made with exosomes isolated from MDA cells (breast cancer cells) in these same cells, where the encapsulated porphyrin showed a higher phototoxicity than its free form (Fuhrmann, Serio, Mazo, Nair, & Stevens, 2014). Once again, this could be the result of the use of non-specific exosomes (not derived from the treated cells), possibly incompatible (little to no affinity) with ARPE-19 cells. For further understanding of these results, future in vivo studies should be performed, preferably with exosomes derived from the same type of cells.

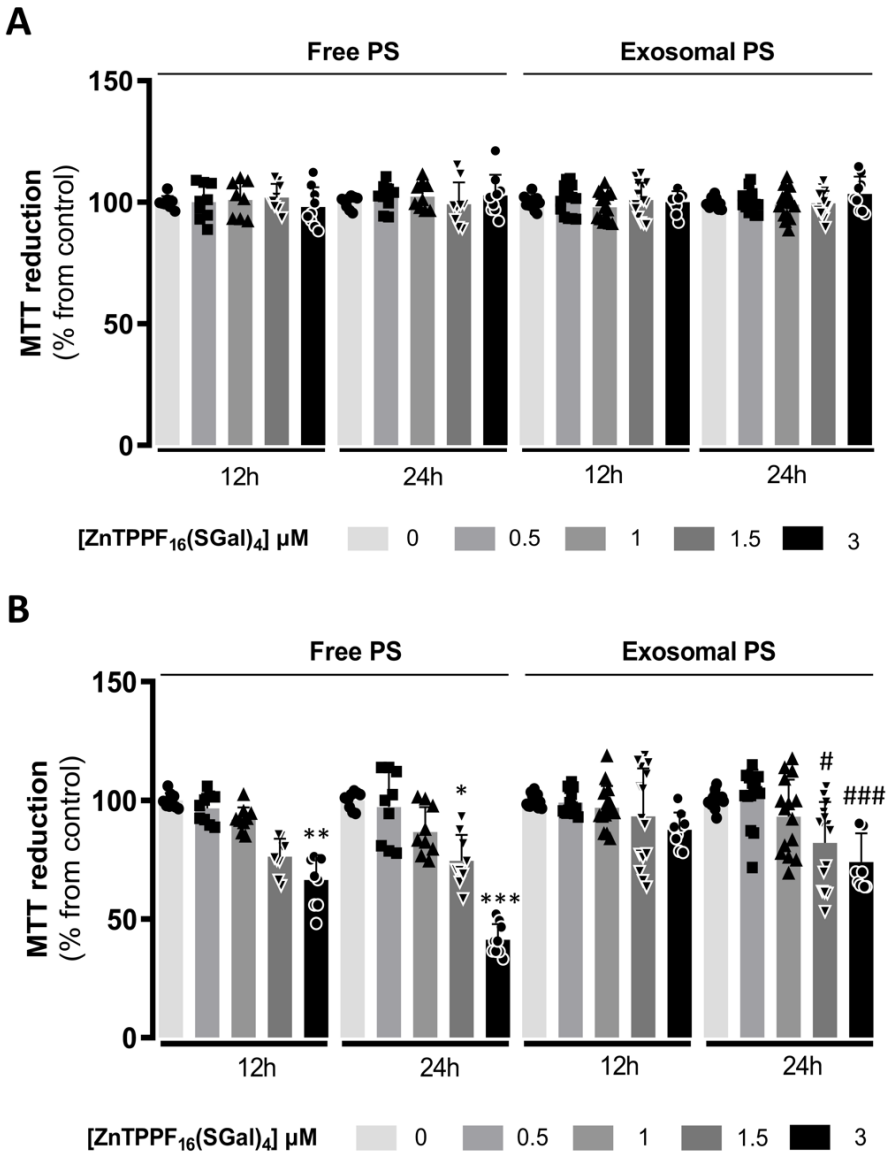

Figure 3.9. $ZnTPPF_{16}(SGal)_4$ and exosomal $ZnTPPF_{16}(SGal)_4$ toxicity in ARPE-19 cells in the dark and after light irradiation. ARPE-19 cells were incubated with $ZnTPPF_{16}(SGal)_4$ at 0.5, 1 and 1.5 mM for 12 and 24 hours in DMEM/F-12, in dark conditions. Cell viability was assessed 24 hours after treatment (dark (A) or after irradiation with LEDs at 8.4 $mW.cm^{-2}$ for 40 min (B)) using the MTT colorimetric assay. The percentage of cytotoxicity was calculated relatively to control cells (cells incubated without PS). Data are the mean value ± S.E.M. of three independent experiments performed in triplicates. Free PS: $^{*}P<0.05$, $^{**}P<0.01$, $^{***}P<0.001$ significantly different from cells incubated in DMEM/F-12, at the same time point. Exosomal PS: $^{\#}P<0.05$, $^{\#\#\#}P<0.001$ significantly different from cells incubated in DMEM/F-12, at the same time point. No significant changes found between the free form of the PS and exosomal PS MTT reduction for the same concentrations and time points. One-way ANOVA followed by Kruskal-Wallis multiple comparison test was performed.

3.7 Laser-induced Choroidal Neovascularization leads to Retinal Lesions

As we intend to assess the effectiveness of PDT with $ZnTPPF_{16}(SGal)_4$ and exosomal $ZnTPPF_{16}(SGal)_4$ *in vivo* soon, we established a laser-induced CNV animal model in our laboratory. Lesions were created by one laser-induced CNV protocol. The mice were anesthetized, their pupils dilated, and CNV induction involved laser burning of Bruch´s membrane at four positions around the optic disc. We did not consider lesions that were bleeding after initial laser burn. The lesions were confirmed by OCT at 3, 7, and 14 days post-laser and fundus fluorescein angiography at 7, and 14 days post-laser. They were found to be in the outer layers of the retina, according to OCT (Fig. 3.10). Fluorescein angiography revealed fluorescein leakage at day 7 (bright spots), which remained unchanged at day 14, indicating the CNV model was successfully induced (Fig. 3.10). Results showed the presence of a bubble in Bruch's membrane after laser burn, thus confirming the success of the laser impact at the RPE (Fig. 3.10B – Day 0). The appearance of fluorescein leakage at days 7 and 14 was another indicator the CNV model was successfully induced. Moreover, these spots matched the thickening of the RPE on cross-sectional retinal images taken from the regions where the rupture of Bruch's membrane occurred (Fig. 3.10B).

Because there are inherent differences between mice and human eyes, no single model can properly recapitulate all features of wet AMD, so this does not constitute a wet AMD model. Besides the fact that mice do not have macula, this model of CNV is a laser trauma model (not spontaneous) based on a wound-healing process that occurs after a Bruch´s membrane damage with laser burning, as described in 1.5, and it is largely reliant on inflammation (Espinosa-Heidmann, et al., 2003). However, it can be a very useful model for the study of CNV treatment, an application already seen in previous studies (e.g., Wolf, Herb, Schramm, & Langmann, 2020). Of note, in this model there is a spontaneous regression of lesions after 14-21 days. This was obviously not observed due to the duration of this experiment (14 days).

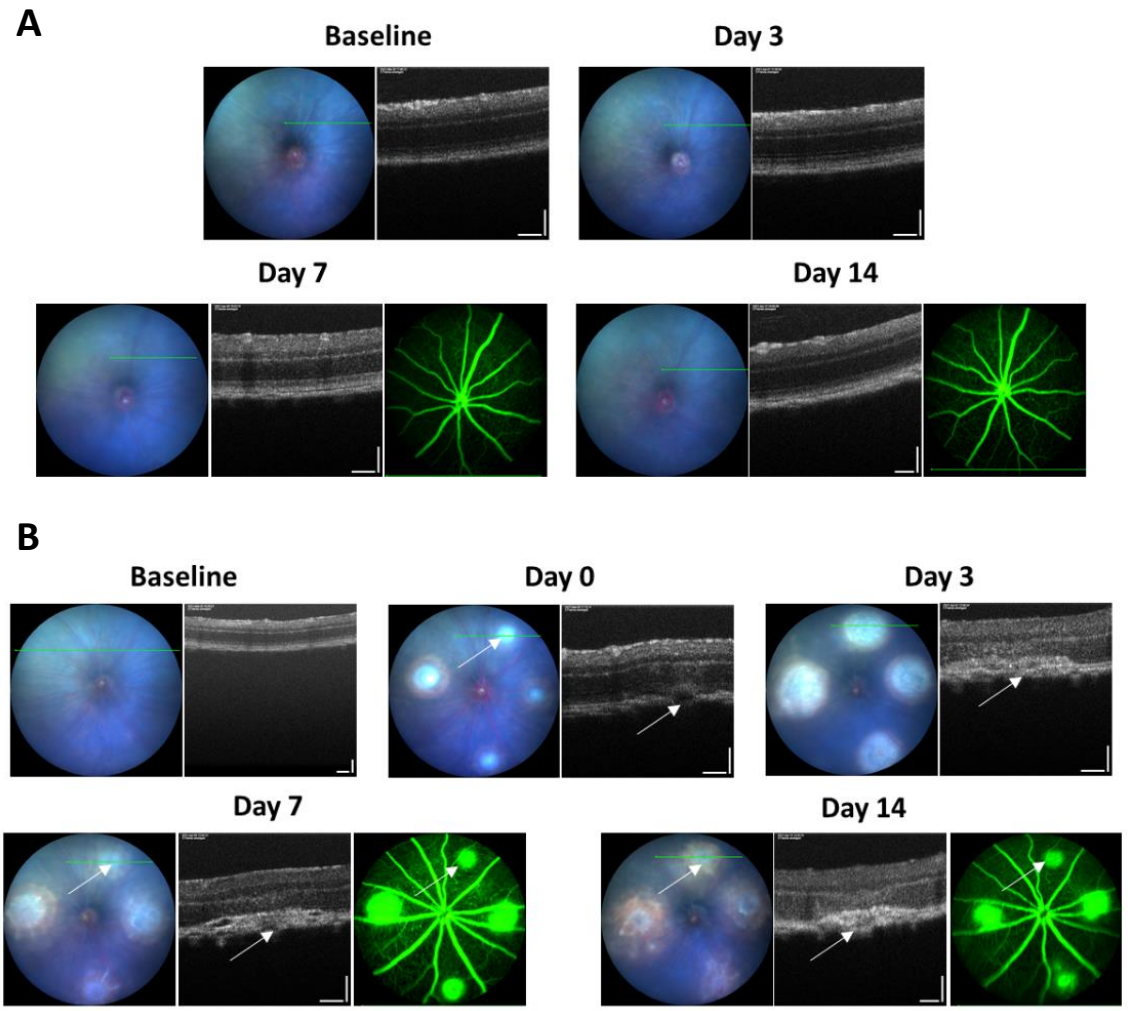

Figure 3.10. Fundus images, OCT and FFA of subretinal lesions. Subretinal lesions were induced using a laser Vitra 2 in wild-type C57BL/6J mice with four burns on the fundus of each eye, with the laser settings of 120 mW power, 50 µm spot size, and 100 ms pulse duration. Representative eye fundus photographs, cross-sectional retinal images and fluorescein angiography images from a (A) control mouse (no laser irradiation) and (B) laser-CNV model.

3.7.1 Immunophenotype of Subretinal Lesions

To further characterize the subretinal lesions, mice were sacrificed at day 14 post-laser, the eyes enucleated and frozen. Eye cross-sections were double-stained for α-SMA and Ki67. α-SMA stains fibrosis and the proliferator marker Ki67 identifies cells in G1 phase, phase S, G2 phase, or mitosis, but not in G0. Ki67 is normally expressed in the nucleus, and its cytoplasmic expression is supposed to signify that the cell is in active mitosis. Ki67 staining was essentially at the cytoplasm of the cells (Fig.3.11). α-SMA stained also in the area of the lesion, suggesting that this area became a fibrotic lesion (Fig. 3.11; arrows). Co-localization of Ki67 and α-SMA was observed on the laser-induced CNV (Fig. 3.11; asterisks).

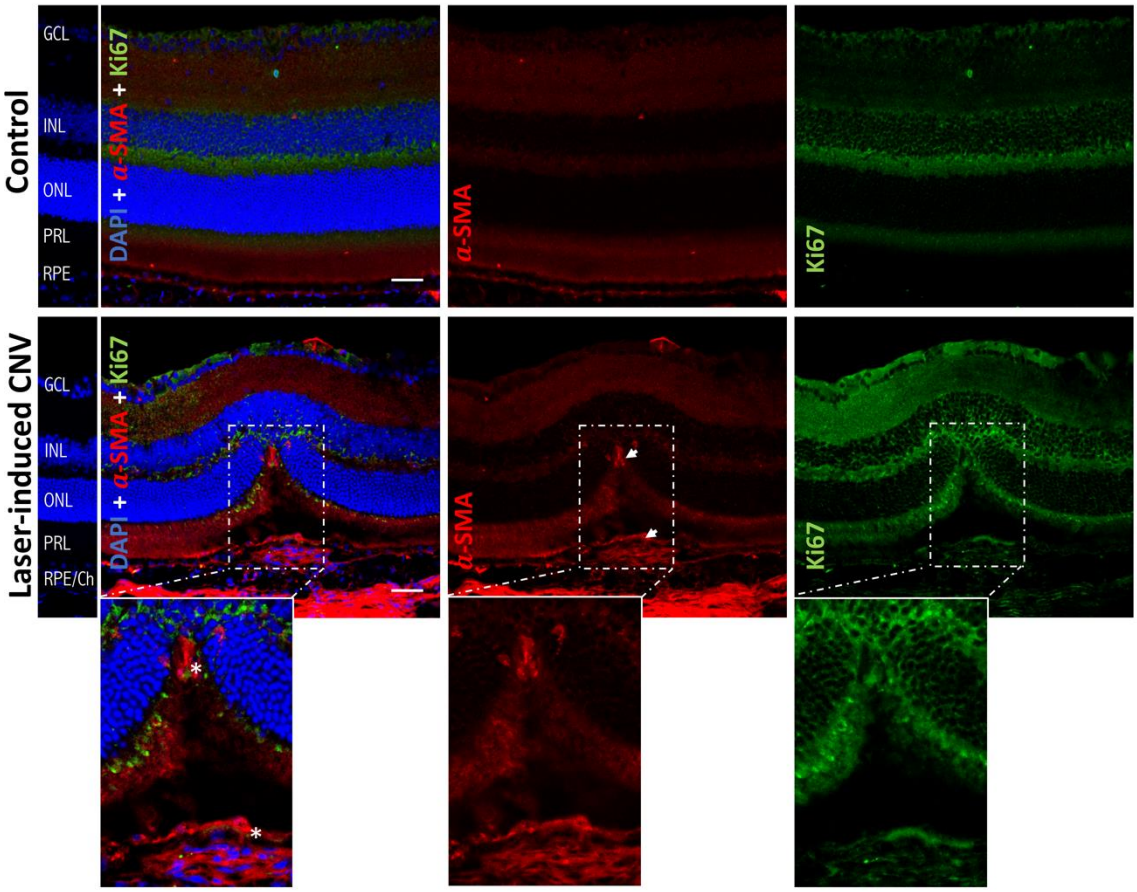

Figure 3.11. Double immunofluorescence staining of α-SMA and Ki67 in cryosections of eyes from laser-induced CNV mice at 14 days p.l. Representative confocal images for control and laser-induced CNV mice, showing α-SMA (red) and Ki67 (green) immunoreactivity and nuclear staining with DAPI (blue) in retinal sections. Scale bar: 20 μm. Legend: GCL - ganglion cell layer; IPL: inner plexiform layer; INL: inner nuclear layer; ONL: outer nuclear layer; PRL: photoreceptor layer.

The results shown in Fig. 3.11 revealed the afore-mentioned co-localization of Ki67 and α-SMA, an indication of newly formed fibrosis, since α-SMA and Ki67 identify fibrosis and proliferating cells, respectively. This fibrosis should be the consequence of a wound healing response to the tissue damage provoked by the CNV (in data not shown, immunostaining of CD31, a marker for endothelial cells, revealed the presence of CNV in some lesions), as reported by Ishikawa (Ishikawa, Kannan, & Hinton, 2015). Hence, this model can also be useful for the study of retinal fibrosis.

Chapter IV

Conclusion and Future Perspectives

This work consisted of the study of a drug delivery system composed by a zinc-porphyrin conjugated with four thiogalactose molecules, $ZnTPPF_{16}(SGal)_4$, and exosomes, to act as drug carriers, as a potential alternative for PDT treatment of fibrosis in wet AMD patients. Exosomes are known to take part in intercellular communication and show affinity to certain tissues, depending on their origin. The inclusion of galactose molecules was an attempt to increase the selectivity to Gal1 and Gal3 since previous studies had shown the expression of Gal1 and Gal3 in angiogenic and fibrogenic processes found in wet AMD.

The photophysical characterization of the PS, specifically its absorption spectrum, photostability and fluorescence, was performed. Results showed the PS exhibits Soret and Q bands characteristic of porphyrins, that it can be described as photostable and that it possesses fluorescence properties (essential for the assessment of drug encapsulation and cellular uptake). The next step was the manufacturing of PS-loaded exosomes, the so-called exosomal PS. This was done successfully, as all exosomal PS preparations revealed some encapsulation efficacy, dependent on the quantity of exosomes and the concentration of PS. Sonication bath led to better encapsulation efficacy than probe sonication.

In vitro studies performed in ARPE-19 cells revealed that free PS had a bigger cellular uptake and phototoxicity in PBS than DMEM/F-12 for 1 and 2 hours (only for the cellular uptake). We postulate that it may be the result of an interaction with FBS. As for the cellular uptake and the toxicity in dark conditions and after light irradiation of free versus exosomal PS for 12 and 24 hours, even though we saw a bigger cellular uptake and phototoxicity for free PS, statistical analysis revealed it was not significantly different to the results with exosomal PS. We suppose it might be an incompatibility between the pig-derived exosomes and the human ARPE-19 cells.

Future research of this alternative treatment for fibrosis in wet AMD should include some improvements. The most important is that it should be performed with exosomes derived from the same animal species and type of cells as the ones in study. Another possible upgrade could be the increase of the incubation period (passive diffusion) during drug encapsulation, as it may result in an even better encapsulation efficacy. Lastly, a greater characterization of the exosomal PS, particularly by 3D imaging, should come as a priority, since it may be important for the understanding of the bond formed by the PS and the exosomes.

The animal model of CNV induced by laser photocoagulation was well established, using previous studies used as a reference. Results showed it was efficient in inducing the rupture of Bruch's membrane, triggering the development of CNV (data not shown revealed possible signs of CNV) and fibrosis (probably provoked by the CNV) in lesion areas. The establishment of an animal model of CNV induced by laser photocoagulation that also presents fibrosis, opens up the possibility to assess the photodynamic effect of both free $ZnTPPF_{16}(SGal)_4$ and exosomal $ZnTPPF_{16}(SGal)_4$.

References

Adrean, S. D., Morgenthein, E., Ghanekar, A., & Ali, F. S. (2020). Subretinal Fibrosis in HARBOR Varies by Choroidal Neovascularization Subtype. *Ophtalmology Retina, 4*(7), pp. 752-754. doi:10.1016/j.oret.2020.02.012

Allen, N. J., & Lyons, D. A. (2018). Glia as architets of central nervous system formation and function. *Science, 362*(6411), pp. 181-185. doi:10.1126/science.aat0473

Ambati, J., Atkinson, J. P., & Gelfand, B. D. (2013). Immunology of age-related macular degeneration. *Nature Reviews Immunology, 13*(6), pp. 438-451. doi:10.1038/nri3459

Antimisiaris, S. G., Mourtas, S., & Marazioti, A. (2018). Exosomes and Exosome-Inspired Vesicles for Targeted Drug Delivery. *Pharmaceutics, 10*(4). pp. 218. doi:10.3390/pharmaceutics10040218

AREDS 2 Research Group (2014). Secondary Analysis of the Effects of Lutein/Zeaxanthin on Age-Related Macular Degeneration Progression. *JAMA Ophtalmology, 132*(2), pp. 142-149. doi:10.1001/jamaophthalmol.2013.7376

Argueso, P., & Panjwani, N. (2011). Focus on Molecules: Galectin-3. *Experimental Eye Research, 92*(1), pp. 2-3. doi:10.1016/j.exer.2010.11.009

Armstrong, R. A., & Cubbidge, R. C. (2019). The Eye and Vision: An Overview. In V. Preedy, & R. Watson, *Handbook of Nutrition, Diet, and the Eye*, pp. 3-10. doi:10.1016/B978-0-12-815245-4.00001-6

Babincová, M., Sourivong, P., & Babinec, P. (2000). Gene transfer-mediated intracellular photodynamic therapy. *Medical Hypotheses, 54*(2), pp. 180-181. doi:10.1054/mehy.1999.0012

Bacigalupo, M. L., Manzi, M., Rabinovich, G. A., & Troncoso, M. F. (2013). Hierarchical and selective roles of galectins in hepatocarcinogenesis, liver fibrosis and inflammation of hepatocellular carcinoma. *World Journal of Gastroenterology, 19*(47), pp. 8831-8849. doi:10.3748/wjg.v19.i47.8831

Balser, C., Wolf, A., Herb, M., & Langmann, T. (2019). Co-inhibition of PGF and VEGF blocks their expression in mononuclear phagocytes and limits neovascularization and leakage in the murine retina. *Journal of Neuroinflammation, 16*. doi:10.1186/s12974-019-1419-2

Banfer, S., & Jacob, R. (2020). Galectins in Intra- and Extracellular Vesicles. *Biomolecules, 10*(9). doi:10.3390/biom10091232

Bei, Y., Das, S., Rodosthenous, R. S., Holvoet, P., Vanhaverbeke, M., Chagas Monteiro, M., Xiao, J. (2017). Extracellular Vesicles in Cardiovascular Theranostics. *Theranostics, 7*(17), pp. 4168-4182. doi:10.7150/thno.21274

Bellavia, D., Raimondi, L., Costa, V., De Luca, A., Carina, V., Maglio, M., Giavaresi, G. (2018). Engineered exosomes: A new promise for the management of musculoskeletal diseases. *Biochimica et Biophysica Acta - General Subjects, 1862*(9), pp. 1893-1901. doi:10.1016/j.bbagen.2018.06.003

Calixto, G. M., Bernegossi, J., de Freitas, L. M., Fontana, C. R., & Chorilli, M. (2016). Nanotechnology-Based Drug Delivery Systems for Photodynamic Therapy of Cancer: A Review. *Molecules, 21*(3). doi:10.3390/molecules21030342

Cardona, A. E., Ransohoff, R. M., & Akassoglou, K. (2013). Patterning and Cell Type Specification in the Developing CNS and PNS. *Comprehensive Developmental Neuroscience, 1*, pp. 803-817. doi:10.1016/B978-0-12-397265-1.00085-X

Chau, H.-F., Xie, C., & Wong, K.-L. (2021). Development of "Smart" Photodynamic Theranostics Agents. *Comprehensive Coordination Chemistry*, pp. 771-786. doi:10.1016/B978-0-08-102688-5.00047-7

Chaya, T., Matsumoto, A., Sugita, Y., Watanabe, S., Kuwahara, R., Tachibana, M., & Furukawa, T. (2017). Versatile functional roles of horizontal cells in the retinal circuit. *Scientific Reports, 7*. doi:10.1038/s41598-017-05543-2

Chuang, K., Fields, M. A., & Priore, L. V. (2017). Potential of Gene Editing and Induced Pluripotent Stem Cells (iPSCs) in Treatment of Retinal Diseases. *Yale Journal of Biology and Medicine, 90*(4), pp. 635-642. PMCID: PMC5733854

Colijn, J. M., Buitendijk, G. H., Prokofyeva, E., Alves, D., Cachulo, M. L., Silva, R., Klaver, C. C. (2017). Prevalence of Age-Related Macular Degeneration in Europe: The Past and the Future. *Ophtalmology, 124*(12), pp. 1753-1763. doi:10.1016/j.ophtha.2017.05.035

Coughlin, B. A., Feenstra, D. J., & Mohr, S. (2017). Vision Research. *Muller cells and diabetic retinopathy, 139*, pp. 93-100. doi:10.1016/j.visres.2017.03.013

Cunha, S., Amaral, M. H., Sousa Lobo, J. M., & Silva, A. C. (2016). Therapeutic Strategies for Alzheimer's and Parkinson's Diseases by Means of Drug Delivery Systems. *Current Medicinal Chemistry, 23*(31), pp. 3618-3631. doi:10.2174/0929867323666160824162401

Daniel, E., Toth, C. A., Grunwald, J. E., Jaffe, G. J., Martin, D. F., Fine, S. L., Maguire, M. G. (2014). Risk of Scar in the Comparison of Age-related Macular Degeneration Treatments Trials. *Ophtalmology, 121*(3), pp. 656-666. doi:10.1016/j.ophtha.2013.10.019

Daniell, M. D., & Hill, J. S. (1991). A History of Photodynamic Therapy. *Australia and New Zealand Journal of Surgery, 61*(5), pp. 340-348. doi:10.1111/j.1445-2197.1991.tb00230.x

Diestelhorst, M., & Grisanti, S. (2002). Photodynamic Therapy to Control Fibrosis in Human Glaucotamous Eyes After Trabeculectomy. *Archives of Ophtalmology, 120*(2), pp. 130-134. doi:10.1001/archopht.120.2.130

Ding, J., Lu, G., Nie, W., Huang, L.-L., Zhang, Y., Fan, W., Xie, H.-Y. (2021). Self-Activatable Photo-Extracellular Vesicle for Synergistic Trimodal Anticancer Therapy. *Advanced Materials, 33*(7). doi:10.1002/adma.202005562

Dobson, J., Fernandes de Queiroz, G., & Golding, J. P. (2017). Photodynamic therapy and diagnosis: Principles and comparative aspects. *The Veterinary Journal, 233*, pp. 8-18. doi:10.1016/j.tvjl.2017.11.012

Donoso, L. A., Vrabec, T., & Kuivaniemi. (2010). The role of complement Factor H in age-related macular degeneration: a review. *Survey of Ophtalmology, 55*(3), pp. 227-246. doi:10.1016/j.survophthal.2009.11.001

Downs, J. C., & Girkin, C. A. (2017). Lamina cribrosa in glaucoma. *Current Opinion in Ophtalmology, 28*(2), pp. 113-119. doi:10.1097/ICU.0000000000000354

Espinosa-Heidmann, D. G., Suner, I. J., Hernandez, E. P., Monroy, D., Csaky, K. G., & Cousins, S. W. (2003). Macrophage depletion diminishes lesion size and severity in experimental choroidal neovascularization. *Investigative Ophtalmology & Visual Science, 44*(8), pp. 3586-3592. doi:10.1167/iovs.03-0038

Fleckenstein, M., Keenan, T. D., Guymer, R. H., Chakravarthy, U., Schmitz-Valckenberg, S., Klaver, C. C., Chew, E. Y. (2021). Age-related macular degeneration. *Nature Reviews Disease Primers, 7*(1). doi:10.1038/s41572-021-00265-2

Fuhrmann, G., Serio, A., Mazo, M., Nair, R., & Stevens, M. M. (2015). Active loading into extracellular vesicles significantly improves the cellular uptake and photodynamic effect of porphyrins. *Journal of Controlled Release, 205*, pp. 35-44. doi:10.1016/j.jconrel.2014.11.029

Gamm, David M. and Albert, Daniel M. (2007). aqueous humour. *Encyclopedia Britannica*, https://www.britannica.com/science/aqueous-humor.

Garcia, J. M., Mendonça, L., Brant, R., Abud, M., Regatieri, C., & Diniz, B. (2015). Stem cell therapy for retinal diseases. *World Journal of Stem Cells, 7*(1), pp. 160-164. doi:10.4252/wjsc.v7.i1.160

Gelfand, B. D., & Ambati, J. (2016). A Revised Hemodynamic Theory of Age-Related Macular Degeneration. *Trends in Molecular Medicine, 22*(8), pp. 656-670. doi:10.1016/j.molmed.2016.06.009

Ghauri, A., Ghauri, I., Elhissi, A. M., & Ahmed, W. (2020). Characterization of cochleate nanoparticles for delivery of the anti-asthma drug beclomethasone dipropionate. *Advances in Medical and Surgical Engineering*, pp. 267-277. doi:10.1016/B978-0-12-819712-7.00014-0

Gong, Y., Li, J., Smith, S. Y., Liu, C.-H., Evans, L., Tian, K. (2015). Optimization of an Image-Guided Laser-Induced Choroidal Neovascularization Model in Mice, *PLOS ONE, 10*(7). doi:10.1371/journal.pone.0132643

Haney, M. J., Klyachko, N. L., Zhao, Y., Gupta, R., Plotnikova, E. G., He, Z., Batrakova, E. V. (2015). Exosome as Drug Delivery Vehicles for Parkinson's Disease Therapy. *Journal of Controlled Release, 207*, pp. 18-30. doi:10.1016/j.jconrel.2015.03.033

Hara, A., Niwa, M., Noguchi, K., Kanayama, T., Niwa, A., Matsuo, M., Tomita, H. (2020). Galectin-3 as a Next-Generation Biomarker for Detecting Early Stage of Various Diseases. *Biomolecules, 10*(3). doi:10.3390/biom10030389

Healthline Editorial Team. (2018). *Optic nerve*. Retrieved from Healthline: https://www.healthline.com/human-body-maps/optic-nerve#1

Heiting, G. (2017). *The Retina: Where Vision Begins*. Retrieved from All About Vision: https://www.allaboutvision.com/resources/retina.htm

Imamoto, Y., & Shichida, Y. (2014). Cone visual pigments. *Biochimica et Biophysica Acta - Bioenergetics, 1837*(5), pp. 664-673. doi:10.1016/j.bbabio.2013.08.009

Ishikawa, K., Kannan, R., & Hinton, D. R. (2015). Molecular mechanisms of subretinal fibrosis in age-related macular degeneration. *Experimental Eye Research, 142*, pp. 19-25. doi:10.1016/j.exer.2015.03.009

Jablonská, E., Kubásek, J., Vojtech, D., Ruml, T., & Lipov, J. (2021). Test conditions can significantly affect the results of in vitro cytotoxicity testing of degradable metallic biomaterials. *Scientific Reports, 11*. doi:10.1038/s41598-021-85019-6

Khanna, S., Komati, R., Elchenbaum, D. A., Hariprasad, I., Ciulla, T. A., & Hariprasad, S. M. (2019). Current and upcoming anti-VEGF therapies and dosing strategies for the treatment of neovascular AMD: a comparative review. *BMJ Open Ophtalmology, 4*(1). doi:10.1136/bmjophth-2019-000398

Kim, A., Beng Ng, W., Bernt, W., & Cho, N.-J. (2019). Validation of Size Estimation of Nanoparticle Tracking Analysis on Polydisperse Macromolecule Assembly. *Scientific Reports, 9*. doi:10.1038/s41598-019-38915-x

Klingeborn, M., Dismuke, W. M., Skiba, N. P., Kelly, U., Stamer, W. D., & Bowes Rickman, C. (2017). Directional Exosome Proteomes Reflect Polarity-Specific Functions in Retinal Pigmented Epithelium Monolayers. *Scientific Reports, 7*. doi:10.1038/s41598-017-05102-9

Kniggendorf, V., Dreyfuss, J. L., & Regatieri, C. V. (2020). Age-related macular degeneration: a review of current therapies and new treatments. *Arquivos Brasileiros de Oftalmologia, 83*(6), pp. 552-561. doi:https://doi.org/10.5935/0004-2749.20200082

Kou, J., Dou, D., & Yang, L. (2017). Porphyrin photosensitizers in photodynamic therapy and its applications. *Oncotarget, 8*(46), pp. 81591-81603. doi:10.18632/oncotarget.20189

Kwiatkowski, S., Knap, B., Przystupski, D., Saczko, J., Kedzierska, E., Knap-Czop, K., Kulbacka, J. (2018). Phtodynamic therapy - mechanisms, photosensitizers and combinations. *Biomedicine & Pharmacotherapy, 106*, pp. 1098-1107. doi:10.1016/j.biopha.2018.07.049

Kwon, Y. H., & Yoo, Y. H. (2017). Loss of Pigmented Epithelial Cells Is Prevented by Autophagy. *Autophagy: Cancer, Other Pathologies, Inflammation, Immunity, Infection, and Aging* , pp. 105-117. doi:10.1016/B978-0-12-805420-8.00003-2

Lambert, V., Lecomte, J., Hansen, S., Blacher, S., Alvarez Gonzalez, M.-L., Struman, I., Noel, A. (2013). Laser-induced choroidal neovascularization model to study age-related macular degeneration in mice. *Nature Protocols, 8*(11), pp. 2197-2211. doi:10.1038/nprot.2013.135

Lima, A. M., Pizzol, C. D., Monteiro, F. B., Creczynski-Pasa, T. B., Andrade, G. P., Ribeiro, A. O., & Perussi, J. R. (2013). Hypericin encapsulated in solid lipid nanoparticles: phototoxicity and photodynamic efficincy. *Journal of Photochemistry and Photobiology B: Biology, 125*, pp. 146-154. doi:10.1016/j.jphotobiol.2013.05.010

Luan, X., Sansanaphongpricha, K., Myers, I., Chen, H., Yuan, H., & Sun, D. (2017). Engineering exosomes as refined biological nanoplatforms for drug delivery. *Acta Pharmacologica Sinica, 38*(6), pp. 754-763. doi:10.1038/aps.2017.12

Macular Photocoagulation Study Group, M. (1982). Argon Laser Photocoagulation for Senile Macular Degeneration. *Archives of Ophtalmology, 100*(6), pp. 912-918. doi:10.1001/archopht.1982.01030030920003

Macular Photocoagulation Study Group, M. (1994). Persistent and Recurrent Neovascularization After Laser Photocoagulation for Subfoveal Choroidal Neovascularization of Age-Related Macular Degeneration. *Archives of Ophtalmology, 112*(4), pp. 489-499. doi:10.1001/archopht.1994.01090160065024

Mahabadi, N., & Khalili, Y. A. (2021). Neuroanatomy, *Retina*. PMID: 31424894

Manero-Rupérez, N., Martínez-Bosch, N., Barranco, L. E., Visa, L., & Navarro, P. (2020). The Galectin Family as Molecular Targets: Hopes for Defeating Pancreatic Cancer. *Cells, 9*(3). doi:10.3390/cells9030689

Matsumoto, J., Shiragami, T., Hirakawa, K., & Yasuda, M. (2015). Water-Solubilization of P(V) and Sb(V) Porphyrins and Their Photobiological Application. *International Journal of Photoenergy, 16*, pp. 1-12. doi:10.1155/2015/148964

Melo, A. (2020). *Photodynamic Therapy with Glycoconjugated Porphyrins for Age-related Macular Degeneration.*

Mendoza-Garcia, J., Sebastian, A., Alonso-Rasgado, T., & Bayat, A. (2015). Ex vivo evaluation of the effect of photodynamc therapy on skin scars and striae distensae. *Photodernatology, Photoimmunology & Photomedicine, 31*(5), pp. 239-251. doi:10.1111/phpp.12180

Miesfeld, J. B., & Brown, N. L. (2019). Eye organogenesis: A hierarchical view of ocular development. *Current Topics in Developmental Biology, 132*, pp. 351-377. doi:10.1016/bs.ctdb.2018.12.008

Munoz, J. L., Bliss, S. A., Greco, S. J., Ramkissoon, S. H., Ligon, K. L., & Rameshwar, P. (2013). Delivery of Functional Anti-miR-9 by Mesenchymal Stem Cell-derived Exosomes to Glioblastoma Multiforme Cells Conferred Chemosensitivity. *Molecular Therapy - Nucleic Acids, 2*(10). doi:10.1038/mtna.2013.60

Nickla, D. L., & Wallman, J. (2010). The Multifunctional Choroid. *Progress in Retinal and Eye Research, 29*(2), pp. 144-168. doi:10.1016/j.preteyeres.2009.12.002

Nishiyama, N., Morimoto, Y., Jang, W.-D., & Kataoka, K. (2009). Design and development of dendrimer photosensitizer-incorporated polymeric micelles for enhanced photodynamic therapy. *Advanced Drug Delivery Reviews, 61*(4), pp. 327-338. doi:10.1016/j.addr.2009.01.004

Ohno, S.-i., Takanashi, M., Sudo, K., Ueda, S., Ishikawa, A., Matsuyama, N., Kuroda, M. (2013). Systemically Injected Exosomes Targeted to EGFR Deliver Antitumor MicroRNA to Breast Cancer Cells. *Molecular Therapy, 21*(1), pp. 185-191. doi:10.1038/mt.2012.180

Ohulchanskyy, T. Y., Roy, I., Goswami, L. N., Chen, Y., Bergey, E. J., Pandey, R. K., Prasad, P. N. (2007). Organically modified silica nanoparticles with covalently incorporated photosensitizer for photodynamic therapy of cancer. *Nano Letters, 9*, pp. 2835-2842. doi:10.1021/nl0714637

Papadopoulos, N., Martin, J., Ruan, Q., Rafique, A., Rosconi, M. P., Shi, E., Wiegand, S. J. (2012). Binding and neutralization of vascular endothelial growth factor (VEGF) and rlated ligands by VEGF Trap, ranibizumab and bevacizumab. *Angiogenesis, 15*(2), pp. 171-185. doi:10.1007/s10456-011-9249-6

Ricci, F., Bandello, F., Navarra, P., Staurenghi, G., Stumpp, M., & Zarbin, M. (2020). Neovascular Age-Related Macular Degeneration: Therapeutic Management and New-Upcoming Approaches. *International Journal of Molecular Sciences, 21*(21). doi:10.3390/ijms21218242

Ruan, Y., Jiang, S., & Gericke, A. (2021). Age-Related Macular Degeneration: Role of Oxidative Stress and Blood Vessels. *International Journal of Molecular Sciences, 22*(3). doi:10.3390/ijms22031296

Ryan, S. J. (1979). The development of an experimental model of subretinal neovascularization in disciform macular degeneration. *Transactions of the American Ophtalmological Society, 77*, pp. 707-745. PMCID: PMC1311723

Selhorst, J., & Chen, Y. (2009). The Optic Nerve. *Seminars in Neurology, 29*(1), pp. 29-35. doi:10.1055/s-0028-1124020

Shahzidi, S., Brech, A., Sioud, M., Li, X., Suo, Z., Nesland, J. M., & Peng, Q. (2013). Lamin A/C cleavage by caspase-6 activation is crucial for apoptotic induction by photodynamic

therapy with hexaminolevulinate in human B-cell lymphoma cells. *Cancer Letters, 339*(1), pp. 25-32. doi:10.1016/j.canlet.2013.07.026

Shang, F. (2017). View of Cellular Biology through the Eye. *Current Molecular Medicine, 17*(4), 247-248. doi:10.2174/1566524017041712071506O2

Singh, N., Srinivasan, S., Muralidharan, V., Roy, R., V, J., & Raman, R. (2017). Prevention of Age-Related Macular Degeneration. *Asia-Pacific Journal of Ophtalmology, 6*(6), pp. 520-526. doi:10.22608/APO.2017416

Son, J., Yang, S. M., Yi, G., Roh, Y. J., Park, H., Park, J. M., Koo, H. (2018). Folate-modified PLGA nanoparticles for tumor-targeted delivery of pheophorbide a in vivo. *Biochemical and Biophysical Research Communications, 498*(3), pp. 523-528. doi:10.1016/j.bbrc.2018.03.013

Song, W. K., Park, K.-M., Kim, H.-J., Lee, J. H., Choi, J., Chong, S. Y., Lanza, R. (2015). Treatment of macular degeneration using embryonic stem cell-derived retinal pigment epithelium: preliminary results in Asian patients. *Stem Cell Reports, 4*(5), pp. 860-872. doi:10.1016/j.stemcr.2015.04.005

Soo Kim, M., Haney, M. J., Zhao, Y., Mahajan, V., Deygen, I., Klyachko, N. L., Batrakova, E. V. (2016). Development of Exosome-encapsulated Paclitaxel to Overcome MDR in Cancer Cells. *Nanomedicine: Nanotechnology, Biology, and Medicine, 12*(3), pp. 655-664. doi:10.1016/j.nano.2015.10.01

Sridhar, M. S. (2018). Anatomy of cornea and ocular surface. *Indian Journal of Ophthalmology, 66*(2), pp. 190-194. doi:10.4103/ijo.IJO_646_17

Takehara, K., Yano, S., Tazawa, H., Kishimoto, H., Narii, N., Mizuguchi, H., Hoffman, R. M. (2017). Eradication of melanoma in vitro and in vivo via targeting with a Killer-Red-containing telomerase-dependent adenovirus. *Cell Cycle, 16*(16), pp. 1502-1508. doi:10.1080/15384101.2016.1249548

Tan, W., Zou, J., Yoshida, S., Jiang, B., & Zhou, Y. (2020). The Role of Inflammation in Age-Related Macular Degeneration. *International Journal of Biological Sciences, 16*(15), pp. 2989-3001. doi:10.7150/ijbs.49890

Thomas, C. J., Mirza, R. G., & Gill, M. K. (2021). Age-Related Macular Degeneration. *Medical Clinics of North America, 105*(3), pp. 473-491. doi:10.1016/j.mcna.2021.01.003

Torricelli, A. A., Singh, V., Santhiago, M. R., & Wilson, S. E. (2013). The Corneal Epithelial Basement Membrane: Structure, Function, and Disease. *Investigative Ophtalmology & Visual Science, 54(9)*, pp. 6390-6400. doi:10.1167/iovs.13-12547

Tram, N. K., & Swindle-Reilly, K. E. (2018). Rheological Properties and Age-Related Changes of the Human Vitreous Humor. *Frontiers in Bioengineering and Biotechnology, 6*. doi:10.3389/fbioe.2018.00199

Vader, P., Mol, E. A., Pasterkamp, G., & Schiffelers, R. M. (2016). Extracellular vesicles for drug delivery. *Advanced Drug Delivery Reviews, 106*, pp. 148-156. doi:10.1016/j.addr.2016.02.006

Vecino, E., Rodriguez, F. D., Ruzafa, N., Pereiro, X., & Sharma, S. C. (2016). Glia-neuron interactions in the mammalian retina. *Progress in Retinal and Eye Research, 51*, pp. 1-40. doi:10.1016/j.preteyeres.2015.06.003

Villa, F., Quarto, R., & Tasso, R. (2019). Extracellular Vesicles as Natural, Safe and Efficient Drug Delivery Systems. *Pharmaceutics, 11*(11). doi:10.3390/pharmaceutics11110557

Wolf, A., Herb, M., Schramm, M., & Langmann, T. (2020). The TSPO-NOX1 axis controls phagocyte-triggered pathological angiogenesis in the eye. *Nature Communications, 11*(1). doi:10.1038/s41467-020-16400-8

Wong, W. L., Su, X., Li, X., Cheung, C. M., Klein, R., Cheng, C.-Y., & Wong, T. Y. (2014). Global prevalence of age-related macular degeneration and disease burden projection for 2020 and 2040: a systematic review and meta-analysis. *The Lancet Global Health, 2*(2), pp. 106-116. doi:10.1016/S2214-109X(13)70145-1

Wu, D., Kanda, A., Liu, Y., Kase, S., Noda, K., & Ishida, S. (2019). Galectin-1 promotes choroidal neovascularization and subretinal fibrosis mediated via epithelial-mesenchymal transition. *The FASEB Journal, 33*(2), pp. 2498-2513. doi:10.1096/fj.201801227R

Wu, Y., Deng, W., & Klinke II, D. J. (2015). Exosomes: Improved methods to characterize their morphology, RNA content, and surface protein biomarkers. *Analyst Journal, 140*(19), pp. 6631-6642. doi:10.1039/c5an00688k

Yao, K., & Ricardo, S. D. (2016). Mesenchymal stem cells as novel micro-ribonucleic acid delivery vehicles in kidney disease. *Nephrology, 21*(5), pp. 363-371. doi:10.1111/nep.12643

Yonekawa, Y., Miller, J. W., & Kim, I. K. (2015). Age-Related Macular Degeneration: Advances in Management and Diagnosis. *Journal of Clinical Medicine, 4*(2), pp. 343-359. doi:10.3390/jcm4020343

Yu, B., Lee, R. J., & Lee, L. J. (2009). Microfluidic Methods for Production of Liposomes. *Methods in Enzymology, 465*, pp. 129-141. doi:10.1016/S0076-6879(09)65007-2

Zeiss, C. J., Tu, D. C., & Treuting, P. (2012). Special Senses Eye. *Comparative Anatomy and Histology*, pp. 395-418. doi:10.1016/B978-0-12-381361-9.00021-4

Zhang, X., & Sivaprasad, S. (2021). Drusen and pachydrusen: the definition, pathogenesis, and clinical significance. *Eye, 35*(1), pp. 121-133. doi:10.1038/s41433-020-01265-4